Quasi-equilibrium states for helical vortices with swirl

Yonghui Xu, Ivan Delbende, Maurice Rossi

▶ **To cite this version:**

Yonghui Xu, Ivan Delbende, Maurice Rossi. Quasi-equilibrium states for helical vortices with swirl. Journal of Fluid Mechanics, 2022, 944, pp.A24. 10.1017/jfm.2022.500 . hal-03811609

HAL Id: hal-03811609

https://hal.sorbonne-universite.fr/hal-03811609v1

Submitted on 10 Jul 2024

HAL is a multi-disciplinary open access archive for the deposit and dissemination of scientific research documents, whether they are published or not. The documents may come from teaching and research institutions in France or abroad, or from public or private research centers.

L'archive ouverte pluridisciplinaire **HAL**, est destinée au dépôt et à la diffusion de documents scientifiques de niveau recherche, publiés ou non, émanant des établissements d'enseignement et de recherche français ou étrangers, des laboratoires publics ou privés.

CrossMark

J. Fluid Mech. (2022), *vol*. 944, A24, doi:10.1017/jfm.2022.500

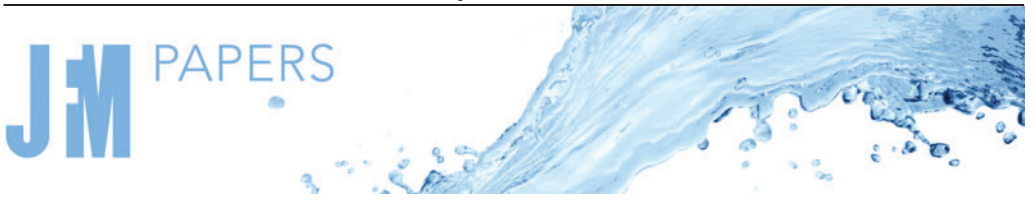

Quasi-equilibrium states for helical vortices with swirl

Yonghui Xu[1,2], **Ivan Delbende**[2,†] **and Maurice Rossi**[2]

[1]Sorbonne Université, Collège Doctoral, 75005 Paris, France

[2]Sorbonne Université, CNRS, UMR 7190, Institut Jean Le Rond d'Alembert, 75005 Paris, France

(Received 20 January 2022; revised 6 April 2022; accepted 19 May 2022)

We present a family of exact equilibrium solutions of the Euler equations consisting of a single helical vortex with an axial flow component along the vortex core. Relations between vorticity, velocity and streamfunction are analytically derived in the inviscid framework and constitute a generalization of relations valid for vortex rings (Batchelor, 1967 *An Introduction to Fluid Dynamics*. Cambridge University Press). Through Navier–Stokes simulations, it is shown that these relations hold for quasi-steady viscous solutions and become independent of the Reynolds number when sufficiently large. We also elaborate a procedure which generates a quasi-equilibrium with prescribed characteristics (circulation, helix radius, helical pitch, vortex core size, swirl level) and compare the obtained state with the results of an asymptotic theory. Finally, we illustrate how a strong axial flow jeopardizes such an evolution towards a quasi-equilibrium.

Key words: general fluid mechanics

1. Introduction

Flow instability studies often require the knowledge of a base flow consisting of an equilibrium state. By equilibrium state, we mean a fixed point of the governing equations, i.e. an exact steady solution of the Navier–Stokes equations. If one excepts spatially uniform and solid-body rotation flows, an unbounded viscous flow without external forcing never remains steady, as its kinetic energy is converted into thermal energy by viscosity. Nevertheless, it is standard to use the classical instability theory for a base solution which is steady for the Euler equations, but unsteady for Navier–Stokes, hence changing slowly over time due to viscous diffusion. This solution will be called a quasi-equilibrium state. When disturbances superimposed on this quasi-equilibrium state are evolving much faster than the diffusion time scale, it is then possible to freeze this time-dependent state and to

† Email address for correspondence: ivan.delbende@sorbonne-universite.fr

© The Author(s), 2022. Published by Cambridge University Press. This is an Open Access article, distributed under the terms of the Creative Commons Attribution licence (https://creativecommons.org/licenses/by/4.0/), which permits unrestricted re-use, distribution, and reproduction in any medium, provided the original work is properly cited.

https://doi.org/10.1017/jfm.2022.500 Published online by Cambridge University Press

treat its instability in a classical manner. The present work is precisely aimed at studying base states which are quasi-equilibrium solutions for a helical vortex with an axial flow component in the core. Such states may be used in instability analyses for helical vortex systems in the wake of wind turbines, marine propellers or helicopter rotors.

Studies on helical vortices go back to the works of Joukowsky & Vetchinkin (1929) and Levy & Forsdyke (1928). The shape of an inviscid pure helical vortex filament remains invariant, as recalled by Kida (1981) using the local induction approximation. Later, Kuibin & Okulov (1998) determined the motion of a helical filament with arbitrary pitches, using the induced velocity provided by Hardin (1982). The results were later extended to multiple helical vortices (Okulov 2004). Torsion effects were characterized by Ricca (1994) and shown to generate a dipolar correction at second order. Finite-core helical vortices were considered by Fukumoto & Okulov (2005): these authors used an asymptotic expansion of the Biot–Savart law allowing them to represent correction terms as a filament of dipoles and of quadrupoles, correcting the monopole filament solution of Hardin. In the context of vortex rings, Fukumoto & Miyazaki (1991) and Fukumoto & Moffatt (2000) showed the influence of such corrections on the ring velocity.

In experiments, it has been verified that helical vortices behind a wind turbine may display an internal jet flow (Quaranta *et al.* 2019). In addition to their rotation around the helical vortex centreline, fluid particles translate along this centreline, as discussed by Okulov & Sørensen (2020). The local flow velocity within the core of helical vortices has been measured in different experiments, namely helical tip vortices generated by a three-bladed rotor (Okulov *et al.* 2019) and a stationary vortex produced in a hydrodynamic vortex chamber (Shtork *et al.* 2020). In both instances, an axial velocity component is found. For straight vortices, the role of such a component on the instability has been studied, causing the famous swirling jet instability (Lessen, Singh & Paillet 1974; Mayer & Powell 1992). In the context of vortices with a core size much smaller than the radius of curvature, i.e. vortex filaments, matched asymptotic expansion techniques were able to introduce an axial flow component within the vortex core (Moore & Saffman 1972; Callegari & Ting 1978). For helical vortices, the internal structure of the core was fully taken into account using asymptotic analysis by Blanco-Rodríguez *et al.* (2015): an axisymmetric (Batchelor 1964) type of vortex core structure was assumed at leading order; a dipolar correction arises at first order, which depends only on the local curvature, and a quadrupolar correction arises at second order, which is associated with local curvature and the non-local strain field.

Away from filament models or asymptotic theory, it is possible to build a steady Euler flow representing an axisymmetric vortex ring. We hereafter use the cylindrical coordinates (r, θ, z) as well as the associated components (u_r, u_θ, u_z) and $(\omega_r, \omega_\theta, \omega_z)$ of the velocity and vorticity fields, while ∂_r, ∂_θ and ∂_z denote partial derivatives with respect to r, θ and z. If $\Psi_S(r, z)$ stands for the Stokes streamfunction, such that $ru_r = -\partial_z\Psi_S$ and $ru_z = \partial_r\Psi_S$, this solution is such that $\omega_\theta = rF_0(\Psi_S)$, where the F_0 is an arbitrary function which satisfies the nonlinear partial differential equation

$$\left(\partial_{rr} - \frac{1}{r}\partial_r + \partial_{zz}\right)\Psi_S(r, z) = -r^2F_0(\Psi_S). \tag{1.1}$$

In the context of steady Euler flow, an azimuthal velocity component can be introduced as well in the core along the vortex axis, leading to new conditions (Batchelor 1967)

$$\omega_\theta = rF(\Psi_S) + \frac{1}{2r}\frac{\mathrm{d}G^2}{\mathrm{d}\Psi_S}(\Psi_S), \quad ru_\theta = G(\Psi_S), \tag{1.2}$$

https://doi.org/10.1017/jfm.2022.500 Published online by Cambridge University Press

where F and G are two arbitrary functions. Given the two functions F and G, an exact Euler equilibrium now satisfies the nonlinear partial differential equation

$$\left(\partial_{rr} - \frac{1}{r}\partial_r + \partial_{zz}\right)\Psi_S(r,z) = -r^2 F(\Psi_S) - \frac{1}{2}\frac{\mathrm{d}G^2}{\mathrm{d}\Psi_S}(\Psi_S). \tag{1.3}$$

As an example, one may quote the family of Hicks (1884) vortex rings, an extension of the spherical Hill vortex with an internal jet.

Our purpose in this communication is threefold: (i) to define constraints generalizing (1.2) for inviscid helical vortex equilibria; (ii) to show that such a family exists and can be obtained as quasi-equilibria of the Navier–Stokes equations; (iii) to provide a procedure to generate by direct numerical simulation (DNS) such a flow with prescribed parameter values (helical pitch, circulation, helix radius, core size and swirl). This latter point is an alternative to the method employed by Brynjell-Rahkola & Henningson (2020).

The paper is organized as follows. In § 2, we briefly present the Navier–Stokes equations for helically symmetric flows written as a generalized vorticity–streamfunction problem. We then derive the conditions which are satisfied by general Euler equilibria for helically symmetric flows with swirl in § 3. Section 4 is devoted to computing quasi-equilibrium states of one helical vortex with prescribed parameters. In § 5, the asymptotic theory provides the field structure for a small self-strain parameter, which is compared with DNS results for some sets of prescribed parameters. Finally in § 6, the effect of the intensity of the initial axial flow is discussed and conclusions are given.

2. Navier–Stokes equations for helical flows

We consider flows with helical symmetry of helical pitch $2\pi L$ along a given axis (in the following, this axis is called the z-axis). Such flows are invariant with respect to a rotation of any angle θ_s around the z-axis coupled with a translation of $L\theta_s$ along the same axis (see for instance Selçuk, Delbende & Rossi 2017). Vortices observed in the wake of turbines and propellers may be approximated in this framework. They are characterized by a circulation Γ and an external velocity U_z^∞, which are respectively the limits of $2\pi r u_\theta$ and u_z as $r \to \infty$. Only the main features of helically symmetric flows are recalled here, yet some new features are also provided. From the cylindrical coordinate basis $(\boldsymbol{e}_r, \boldsymbol{e}_\theta, \boldsymbol{e}_z)$, one defines an orthonormal Beltrami basis $(\boldsymbol{e}_r, \boldsymbol{e}_\varphi, \boldsymbol{e}_B)$, where $\boldsymbol{e}_B$ is directed along the tangent of helical lines $\varphi \equiv \theta - z/L = \mathrm{cst}$, and $\boldsymbol{e}_\varphi = \boldsymbol{e}_B \times \boldsymbol{e}_r$. Only two fields are necessary to describe the flow dynamics of helically symmetric flows, namely $u_B \equiv \boldsymbol{e}_B \cdot \boldsymbol{u}$ and $\omega_B \equiv \boldsymbol{e}_B \cdot \boldsymbol{\omega}$. In addition, both fields are space dependent only via variables r and φ. Incompressibility imposes the existence of a streamfunction $\Psi(r,\varphi,t)$ such that $ru_r = \partial_\varphi \Psi$ and $u_\varphi = -\alpha(r)\partial_r \Psi$, where $\alpha(r) \equiv (1 + r^2/L^2)^{-1/2}$ and ∂_φ denotes the partial derivative with respect to φ. This streamfunction depends on ω_B and u_B through

$$-\mathbb{L}\Psi = \omega_B - \frac{2\alpha^3}{L}u_B, \quad \text{where } \mathbb{L}(\bullet) \equiv \frac{1}{r\alpha}\partial_r[r\alpha^2\partial_r(\bullet)] + \frac{1}{r^2\alpha}\partial_{\varphi\varphi}(\bullet), \tag{2.1}$$

the operator $\mathbb{L}$ being a generalized Laplace operator. Instead of u_B, an equivalent velocity denoted by u_H can be used, defined by

$$u_H \equiv \frac{u_B}{\alpha} - C_\infty, \quad \text{with } C_\infty \equiv \frac{\Gamma}{2\pi L} + U_z^\infty. \tag{2.2}$$

Assuming that the vorticity is localized in the (r,φ) plane – this occurs for instance when one or several helical vortices are present, u_H must vanish away from the vorticity region.

https://doi.org/10.1017/jfm.2022.500 Published online by Cambridge University Press

Indeed, u_H is bound to be constant since $\partial_r u_H = -\omega_\varphi/\alpha$ and $\partial_\varphi u_H = r\omega_r$, and this constant is zero by construction since $u_B/\alpha \to C_\infty$ as $r \to \infty$.

A first dynamical equation can be written for u_H by projecting the Navier–Stokes equations

$$\frac{\partial \boldsymbol{u}}{\partial t} + \boldsymbol{\omega} \times \boldsymbol{u} = -\boldsymbol{\nabla} H - \nu\, \boldsymbol{\nabla} \times \boldsymbol{\omega} \tag{2.3}$$

on $\boldsymbol{e}_B$ and dividing by α. In (2.3), ν stands for the kinematic viscosity and H for the pressure head $p\upsilon + \boldsymbol{u}^2/2$, p denoting the pressure field and υ the specific volume of the fluid. For any scalar function G displaying helical symmetry, the property $\boldsymbol{e}_B \cdot \boldsymbol{\nabla} G = 0$ holds. Applying this property to H yields

$$\partial_t u_H + NL_u = \nu VT_u, \tag{2.4}$$

where the viscous term is given by

$$VT_u \equiv -\frac{1}{\alpha}\boldsymbol{e}_B \cdot [\boldsymbol{\nabla} \times \boldsymbol{\omega}] = \frac{1}{\alpha}\mathbb{L}u_H - \frac{2}{L}\alpha\omega_B \tag{2.5}$$

and the nonlinear term by

$$NL_u = \frac{1}{\alpha}\boldsymbol{e}_B \cdot [\boldsymbol{\omega} \times \boldsymbol{u}] = \frac{1}{\alpha}[\omega_r\, u_\varphi - \omega_\varphi\, u_r] = \frac{u_\varphi}{\alpha r}\partial_\varphi u_H + u_r \partial_r u_H. \tag{2.6}$$

This nonlinear term can be rewritten using the Jacobian $J(f, g)$

$$NL_u = J(u_H, \Psi) \quad \text{with } J(f, g) \equiv \frac{1}{r}\left(\partial_r f\, \partial_\varphi g - \partial_\varphi f\, \partial_r g\right). \tag{2.7}$$

The dynamical equation for ω_B is obtained by projecting the rotational of (2.3) on $\boldsymbol{e}_B$

$$\partial_t \omega_B + NL_\omega = \nu VT_\omega, \tag{2.8}$$

where the viscous term is given by

$$VT_\omega \equiv -\boldsymbol{e}_B \cdot \boldsymbol{\nabla} \times [\boldsymbol{\nabla} \times \boldsymbol{\omega}] = \mathbb{L}(\frac{\omega_B}{\alpha}) - \left(\frac{2\alpha^2}{L}\right)^2 \omega_B + \frac{2\alpha^2}{L}\mathbb{L}(u_H). \tag{2.9}$$

The nonlinear term takes the form

$$NL_\omega \equiv \boldsymbol{e}_B \cdot \boldsymbol{\nabla} \times \boldsymbol{a} = \frac{1}{r\alpha}[\partial_r(r\alpha a_\varphi) - \partial_\varphi a_r] + \frac{2\alpha^2}{L}a_B, \tag{2.10}$$

where (a_B, a_r, a_φ) are the helical components of the Lamb vector $\boldsymbol{a} = \boldsymbol{\omega} \times \boldsymbol{u}$. In (2.10), quantity NL_ω reads

$$NL_\omega = \frac{1}{r\alpha}[\partial_r(r\alpha\omega_B u_r) + \partial_\varphi(\omega_B u_\varphi)] + \frac{2\alpha^2}{L}(\omega_r u_\varphi - \omega_\varphi u_r) + \frac{2\alpha^3}{L^2}(u_H + C_\infty)\partial_\varphi u_H \tag{2.11}$$

and can be simplified using incompressibility yielding the compact expression

$$NL_\omega = \frac{1}{\alpha}J(\alpha\omega_B, \Psi) + \frac{2\alpha^3}{L}J(u_H, \Psi) + \frac{\alpha^3}{L^2}\partial_\varphi[(u_H + C_\infty)^2]. \tag{2.12}$$

The two governing equations (2.4) and (2.8) turn out to be a generalization of the standard two-dimensional ψ–ω, namely a Ψ–ω_B–u_H formulation defined by relations (2.4)–(2.7) for $u_H(r, \varphi, t)$, relations (2.8)–(2.12) for $\omega_B(r, \varphi, t)$, together with the streamfunction $\Psi(r, \varphi, t)$ slaved at any time to these two variables through (2.1).

https://doi.org/10.1017/jfm.2022.500 Published online by Cambridge University Press

3. Inviscid equilibria of helical vortices with swirl

In this section, we are looking for the conditions satisfied by an Euler equilibrium solution which is helically symmetric. Generally, such an inviscid solution is not steady but rotating at angular velocity Ω_0 around the z-axis. This equilibrium is governed by (2.4) and (2.8) in which the viscous terms (2.5) and (2.9) are neglected, leading to

$$\partial_t u_H + J(u_H, \Psi) = 0, \tag{3.1}$$

and

$$\partial_t(\alpha\omega_B) + J(\alpha\omega_B, \Psi) + \frac{2\alpha^4}{L} J(u_H, \Psi) + \frac{\alpha^4}{L^2}\partial_\varphi[(u_H + C_\infty)^2] = 0. \tag{3.2}$$

In the reference frame (T) translating along the z-axis at velocity $U_0\boldsymbol{e}_z \equiv -\Omega_0 L\boldsymbol{e}_z$, this inviscid state becomes a steady solution characterized by the following fields

$$\left.\begin{aligned} u_B^{(T)} &= u_B - \alpha U_0, \\ u_\varphi^{(T)} &= u_\varphi + \alpha U_0 r/L, \\ u_r^{(T)} &= u_r. \end{aligned}\right\} \tag{3.3}$$

Since $z^{(T)} = z - U_0 t$, the variable $\varphi^{(T)}$ associated with the translating frame (T) is defined by

$$\varphi^{(T)} \equiv \theta - \frac{z^{(T)}}{L} = \theta - \frac{z}{L} + \frac{U_0 t}{L} = \varphi + \frac{U_0 t}{L}. \tag{3.4}$$

Since $U_z^{\infty(T)} = U_z^\infty - U_0$, neither quantity ω_B nor quantity u_H depend on the reference frame, as

$$u_H{}^{(T)} = \frac{u_B^{(T)}}{\alpha} - \left(U_z^{\infty(T)} + \frac{\Gamma}{2\pi L}\right) = u_H. \tag{3.5}$$

By contrast, the streamfunction is modified according to

$$\Psi^{(T)} = \Psi - \frac{U_0}{L}\frac{r^2}{2} = \Psi + \frac{1}{2}\Omega_0 r^2, \tag{3.6}$$

which imposes

$$J(u_H, \Psi) = J(u_H, \Psi^{(T)}) + \frac{U_0}{L} J\left(u_H, \frac{1}{2}r^2\right) = J(u_H, \Psi^{(T)}) - \frac{U_0}{L}\partial_{\varphi^{(T)}} u_H. \tag{3.7}$$

Using the identity

$$\partial_t u_H(r, \varphi, t) = \left(\partial_t + \frac{U_0}{L}\partial_{\varphi^{(T)}}\right) u_H(r, \varphi^{(T)}, t), \tag{3.8}$$

(3.1), re-written for a steady state ($\partial_t = 0$) in the translating frame, becomes

$$J(u_H, \Psi^{(T)}) = 0. \tag{3.9}$$

As a consequence, velocity u_H is a constant on any streamline $\Psi^{(T)} = \text{cst}$.

https://doi.org/10.1017/jfm.2022.500 Published online by Cambridge University Press

Similarly, (3.2) for the same steady state yields

$$J(\alpha\omega_B, \Psi^{(T)}) + \frac{\alpha^4}{L^2}\partial_{\varphi^{(T)}}[(u_H + C)^2] = 0, \quad \text{with } C \equiv C_\infty - U_0. \tag{3.10}$$

Note that $u_H + C = u_B^{(T)}/\alpha$. Equation (3.9) imposes

$$J(\alpha^2(u_H + C), \Psi^{(T)}) + \frac{2\alpha^4}{L^2}(u_H + C)\partial_{\varphi^{(T)}}\Psi^{(T)} = 0, \tag{3.11}$$

hence

$$-\frac{\mathrm{d}(u_H + C)}{\mathrm{d}\Psi^{(T)}}J(\alpha^2(u_H + C), \Psi^{(T)}) - \frac{\alpha^4}{L^2}\partial_{\varphi^{(T)}}[(u_H + C)^2] = 0. \tag{3.12}$$

Due to (3.9), one can also derive

$$\begin{aligned}\frac{\mathrm{d}(u_H + C)}{\mathrm{d}\Psi^{(T)}}J(\alpha^2(u_H + C), \Psi^{(T)}) + J\left(-\frac{\alpha^2}{2}\frac{\mathrm{d}(u_H + C)^2}{\mathrm{d}\Psi^{(T)}}, \Psi^{(T)}\right)\\ = -\alpha^2(u_H + C)J\left(\frac{\mathrm{d}(u_H + C)}{\mathrm{d}\Psi^{(T)}}, \Psi^{(T)}\right) = 0.\end{aligned} \tag{3.13}$$

Summing relations (3.10), (3.12) and (3.13) yields

$$J(\varpi, \Psi^{(T)}) = 0, \quad \text{where } \varpi \equiv \alpha\omega_B - \frac{\alpha^2}{2}\frac{\mathrm{d}(u_H + C)^2}{\mathrm{d}\Psi^{(T)}}, \tag{3.14}$$

which indicates that quantity ϖ is a constant on any streamline $\Psi^{(T)} = \text{cst}$. Equations (3.14) and (3.9) show that, in the reference frame in which the flow is steady, there exist two functions f and g such that

$$\omega_B = \frac{1}{\alpha}f(\Psi^{(T)}) + \frac{\alpha}{2}\frac{\mathrm{d}\,g^2}{\mathrm{d}\,\Psi^{(T)}}, \quad \frac{u_B^{(T)}}{\alpha} = u_H + C = g(\Psi^{(T)}). \tag{3.15a,b}$$

The above relations for helical equilibria extend the relation (1.2) valid for axisymmetric equilibria of the Euler equations, which is recovered in the limit $L \to 0$, since then $\alpha \sim 1/r$ and $\boldsymbol{e}_B \to \boldsymbol{e}_\theta$.

In the following section, we check that conditions (3.15*a*,*b*) are met for viscous quasi-steady helical equilibria reached at high Reynolds number.

4. Viscous quasi-steady states

Locally, a helical vortex with large helical pitch $2\pi L$ can be approximated by a two-dimensional vortex with three velocity components subjected to a strain originating from the remaining part of the vortex. On the one hand, it is known that, when subjected to an external potential flow, a pure two-dimensional axisymmetric vortex evolves by emitting filaments during a transient stage called the relaxation stage, rapidly reaching a slightly elliptic state if the external strain is small with respect to the characteristic vorticity of the vortex (Jiménez, Moffatt & Vasco 1996; Le Dizès & Verga 2002). Thereafter, it approaches a slightly deformed Gaussian profile which evolves on a slow diffusion time scale, i.e. a quasi-equilibrium state. On the other hand, a two-dimensional initial flow with three velocity components evolves towards a viscous Batchelor vortex (Rossi 2000). As a consequence, it is reasonable to assume that a similar process occurs for a helical

https://doi.org/10.1017/jfm.2022.500 Published online by Cambridge University Press

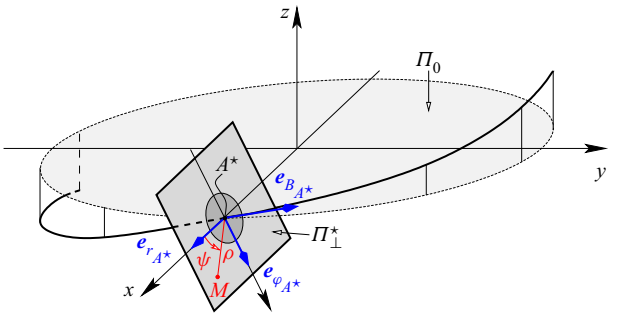

Figure 1. Geometry for building the initial condition.

vortex at finite L, for which the potential flow deforming the vortex core comes from the three-dimensional geometry of the vortex itself. After a rapid relaxation process, a helical vortex with thin core evolves towards a generic quasi-equilibrium helical state. The present section describes this relaxation process, and checks that a quasi-equilibrium is indeed reached. In addition, one explains how to prepare such a final state with prescribed parameters.

4.1. *Initial helical tube*

We search for an initial flow which is helically symmetric along the z-direction, of spatial period $2\pi L$ and characterized by a compact vorticity field, such that $\boldsymbol{\omega}$ tends at least exponentially to zero away from a given helical line.

Let us first define this helical line. As illustrated in figure 1, the line intersects the $z = 0$ plane (thereafter called Π_0) at a point $\mathrm{A}^\star$ defined by its cylindrical coordinates $r_{\mathrm{A}^\star}$ and $\theta_{\mathrm{A}^\star}$. The angle is set to $\theta_{\mathrm{A}^\star} = 0$ without loss of generality. This helical line is thus located at

$$\boldsymbol{x}(\theta_s) = r_{\mathrm{A}^\star}\boldsymbol{e}_r(\theta_s) + L\theta_s\boldsymbol{e}_z, \quad \theta_s \in \mathbb{R}. \tag{4.1}$$

The plane perpendicular to this helical line at point $\mathrm{A}^\star$ is called the plane $\Pi^\star_\perp$. The unit vector $\boldsymbol{e}_{B_{\mathrm{A}^\star}}$ defines the upward normal vector to plane $\Pi^\star_\perp$

$$\boldsymbol{e}_{B_{\mathrm{A}^\star}} = \alpha(r_{\mathrm{A}^\star})\left[\boldsymbol{e}_z + \frac{r_{\mathrm{A}^\star}}{L}\boldsymbol{e}_\theta(0)\right]. \tag{4.2}$$

In this plane, a Cartesian basis $(\boldsymbol{e}_{r_{\mathrm{A}^\star}}, \boldsymbol{e}_{\varphi_{\mathrm{A}^\star}})$ is defined as well

$$\boldsymbol{e}_{r_{\mathrm{A}^\star}} \equiv \boldsymbol{e}_r(0), \quad \boldsymbol{e}_{\varphi_{\mathrm{A}^\star}} \equiv \alpha(r_{\mathrm{A}^\star})\left[\boldsymbol{e}_\theta(0) - \frac{r_{\mathrm{A}^\star}}{L}\boldsymbol{e}_z\right], \tag{4.3a,b}$$

associated with local polar coordinates (ρ, ψ) centred at point $A^\star$ with local basis $(\boldsymbol{e}_\rho, \boldsymbol{e}_\psi)$

$$\boldsymbol{e}_\rho = \cos\psi\ \boldsymbol{e}_{r_{\mathrm{A}^\star}} + \sin\psi\ \boldsymbol{e}_{\varphi_{\mathrm{A}^\star}}, \quad \boldsymbol{e}_\psi = \cos\psi\ \boldsymbol{e}_{\varphi_{\mathrm{A}^\star}} - \sin\psi\ \boldsymbol{e}_{r_{\mathrm{A}^\star}}. \tag{4.4a,b}$$

Practically, the initial condition is a thin-core vortex along the helical line: one chooses a compact profile for $\omega_B(\rho, \psi)$ and for $u_H(\rho, \psi)$ around point $A^\star$. This ensures that ω_φ and ω_r are also compact, a crucial issue. For instance, one assumes axisymmetric profiles similar to the Batchelor vortex

$$\omega_B(\rho) = \omega_B^\star \exp\left(-\frac{\rho^2}{a^{\star 2}}\right), \quad u_H(\rho) = u_H^\star \exp\left(-\frac{\rho^2}{a^{\star 2}}\right), \tag{4.5a,b}$$

where quantities $\omega_B^\star$, $u_H^\star$ and core size $a^\star$ are three dimensional constants. From these profiles in the plane $\Pi^\star_\perp$ as well as the values of the helix radius $r_{\mathrm{A}^\star}$ and reduced pitch

https://doi.org/10.1017/jfm.2022.500 Published online by Cambridge University Press

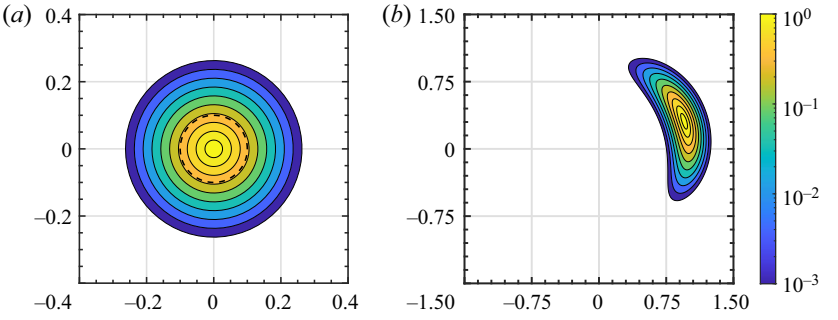

Figure 2. Contours of ω_B/ω_{Bmax} for case A (see text) (*a*) in plane $\Pi_\perp^\star$ and (*b*) in plane Π_0. The dashed circle in (*a*) represents the initial vortex core size $\rho = a^\star$. Contour levels ω_p are given by $\sqrt{-\log(\omega_p)} = \frac{1}{10}p\sqrt{\log(10^3)}$, with $p = 1, \ldots, 10$.

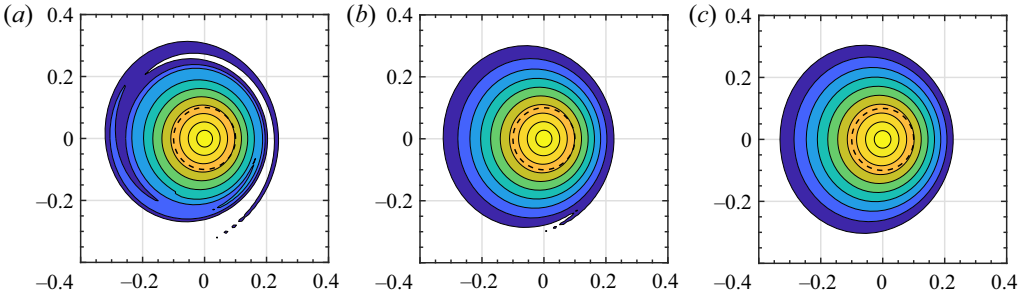

Figure 3. Case A at $t = 4$, 10 and 20: contours of $\omega_B/\omega_{Bmax}(t)$ in plane $\Pi_\perp(t)$. Contours levels are as defined in figure 2.

L, it is possible to compute the initial fields $\omega_B(r, \varphi)$ and $u_H(r, \varphi)$ on the Π_0 plane used in simulations. To do so, we establish the connections between (r, φ) given by a point in Π_0 and the polar radius ρ of the corresponding point in $\Pi_\perp^\star$, using invariances along the lines $\varphi = \theta - z/L = \text{cst}$ (details of such a procedure can be found in Selçuk *et al.* 2017, Appendix A). Let us consider an initial condition called case A characterized by circulation $\Gamma = 1$, initial helix radius $r_{A^\star} = 1$, reduced pitch $L = 0.3$, initial core size $a^\star = 0.1$ and initial axial flow intensity $u_H^\star = 1$. This yields $\omega_B^\star = 32.68$. On the $\Pi_\perp^\star$ plane, the fields are hence axisymmetric and Gaussian (figure 2*a*) whereas in the Π_0 plane, they take a bean-like shape (figure 2*b*).

4.2. *Reaching a viscous helical quasi-equilibrium state*

The Navier–Stokes equations with helical symmetry are integrated over time starting from the previous initial condition (case A). The numerical code uses a polar grid in a circular sub-domain of plane Π_0; it implements the generalized Ψ–ω_B–u_H formulation described in § 2, with second-order finite differences along r, Fourier expansions along φ, second-order time discretization and fully implicit viscous terms (Delbende, Rossi & Daube 2012). Kinematic viscosity is set to $\nu = 1.59 \times 10^{-5}$, so that the Reynolds number $Re \equiv \Gamma/(2\pi\nu)$ is 10^4. It can be observed (see figure 3 for ω_B, and 4 for u_H) that filaments are emitted during the early relaxation stage (see $t = 4$), and then quickly dissipate ($t = 10$) while the vortex becomes quasi-steady ($t = 20$).

https://doi.org/10.1017/jfm.2022.500 Published online by Cambridge University Press

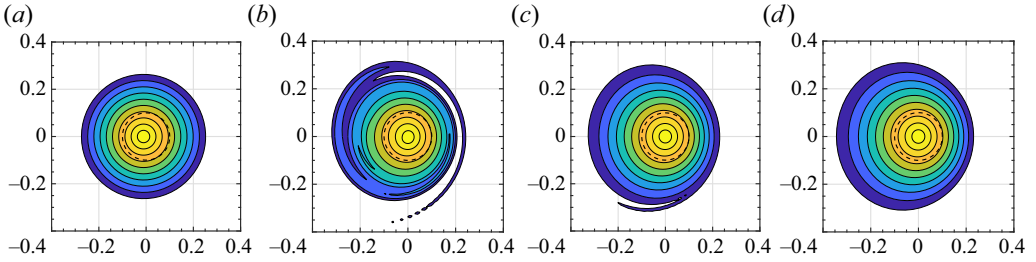

Figure 4. Case A at $t = 0$, 4, 10 and 20: contours of u_H/u_{Hmax} in plane $\Pi_\perp(t)$. Contours levels are defined in the same way as in figure 2 for ω_B/ω_{Bmax}.

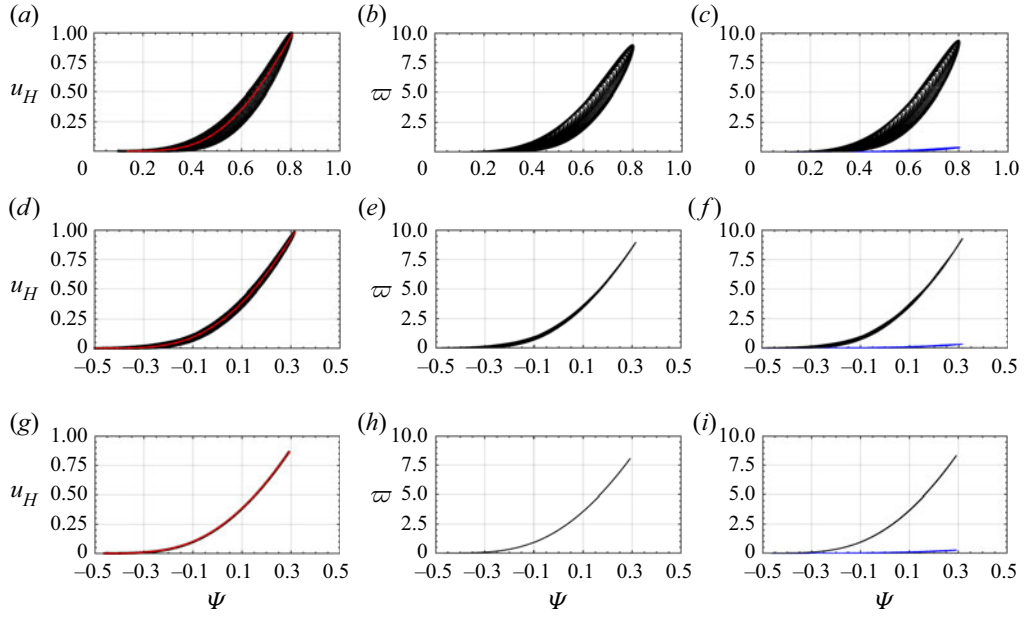

Figure 5. Case A: scatterplots at times $t = 0$ (*a–c*), $t = 2$ (*d–f*) and $t = 20$ (*g–i*): (*a*,*d*,*g*) u_H vs Ψ (the red curve is an estimate of $g(\Psi)$ obtained via formula (A3)); (*b*,*e*,*h*) ϖ vs Ψ; (*c*,*f*,*i*) $\alpha\omega_B$ (black dots) and $\alpha^2 \mathrm{d}(u_H + C)^2/\mathrm{d}\Psi$ (blue dots) vs Ψ. Note that only grid points such that $\omega_B/\omega_{B\,max} > 10^{-3}$ have been represented.

We check how the DNS solution approaches an Euler equilibrium using conditions (3.15*a*,*b*). First, we determine the translating reference frame: velocity $U_0(t)$ is computed by the best correlation of the vorticity field between successive time steps. Second, the streamfunction $\Psi^{(T)}$ in the translating frame is computed using (3.6). From now on, we only consider streamfunction $\Psi^{(T)}$ which will be simply denoted as Ψ. Figure 5(*a*,*d*,*g*) displays scatterplots of u_H vs Ψ at several times for case A. As time increases, it is observed that the points converge to a single continuous curve, supporting the existence of the function g such that $u_H = g(\Psi)$. The second condition (3.15*a*,*b*) requires the derivative $\mathrm{d}u_H/\mathrm{d}\Psi$, a quantity which is defined only if a steady state is reached. A procedure is proposed in Appendix A to provide an estimate value for this derivative (see formula (A4)) during the whole time evolution, that converges to the exact value when the quasi-steady state is reached. In figure 5(*b*,*e*,*h*), scatterplots of quantity ϖ vs Ψ are found to support the existence of a function f such that $\varpi = f(\Psi)$.

https://doi.org/10.1017/jfm.2022.500 Published online by Cambridge University Press

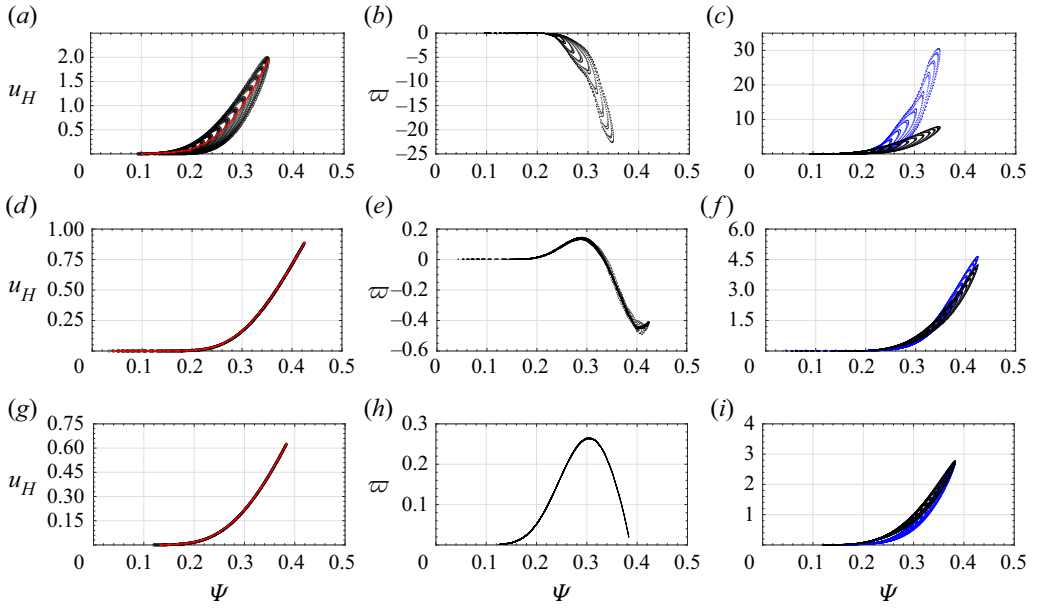

Figure 6. Same as figure 5 but for case B (see text) plotted at times $t = 0$ (*a–c*), $t = 50$ (*d–f*) and $t = 100$ (*g–i*).

For case A, however, quantity $\alpha\omega_B$ dominates the value ϖ (see figure 5*c*,*f*,*i*): when the jet component is weak, quantity ϖ almost equals $\alpha\omega_B$, which visually becomes a function of Ψ. We present a second simulation (case B) where the jet component is initially more intense: circulation $\Gamma = 1$, initial helix radius $r_{A^\star} = 1$, reduced pitch $L = 1.5$, initial core size $a^\star = 0.2$ and initial axial flow intensity $u_H^\star = 2$. This yields $\omega_B^\star = 9.52$. The Reynolds number is set to $Re = 10^3$. As time evolves, velocity u_H converges to a function of Ψ (see figures 6*a*,*d*,*g* and 6*b*,*e*,*h*). For case B, partial quantities $\alpha\omega_B$ and $\alpha^2 \mathrm{d}(u_H + C)^2/\mathrm{d}\Psi$ have same orders of magnitude (see figure 6*c*,*f*,*i*) so that the corresponding points remain scattered even at late times. Quantity $\varpi = \alpha\omega_B - \alpha^2 \mathrm{d}(u_H + C)^2/\mathrm{d}\Psi$, however, clearly converges towards a function of Ψ (see figure 6*b*,*e*,*h*). This fully confirms the new finding expressed by relations (3.15*a*,*b*).

Figure 7 represents the relation reached in the quasi-equilibrium state between ϖ and u_H. When axial vorticity dominates over axial velocity (figure 7*a*) there is a linear relationship between $\varpi \approx \alpha\omega_B$ and u_H. When both effects have comparable orders of magnitude, this relation becomes highly nonlinear (figure 7*b*). Finding an analytical expression for such relations remains an open issue.

4.3. *Determination of the centre of the helical vortex*

The above results suggest that, in order to characterize the structure of the vortex, the most convenient way is to select the point of maximum Ψ as a centre for the vortex. When this quantity is available, one looks for the point A where Ψ reaches a maximum in the plane Π_0 (for most single helical vortices, this point is unique), and one defines the associated plane $\Pi_\perp$ in a similar way as $\Pi_\perp^\star$ is defined from A* (see above in § 4.1 and figure 1). Since the field Ψ depends on (r, φ), there is a one-to-one relation between its values in the plane $\Pi_\perp$ and in the plane Π_0. Consequently, it also reaches a maximum in the $\Pi_\perp$ plane at point A. Other properties can be also useful to locate this central point. Since $ru_r = \partial_\varphi \Psi$

https://doi.org/10.1017/jfm.2022.500 Published online by Cambridge University Press

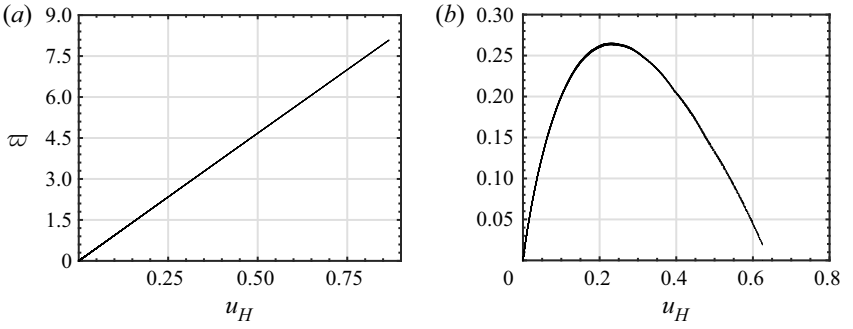

Figure 7. Quantity ϖ as a function of u_H at quasi-equilibrium for (*a*) case A (see figure 5) and (*b*) case B (see figure 6).

	$\alpha\omega_B$	u_H	Ψ
Case A	1.008	1.008	1.008
Case B	0.983	1.015	1.015

Table 1. Radial location of the maximum for different quantities, as measured in the DNS for cases A and B.

and $u_\varphi = -\alpha(r)\partial_r\Psi$, velocity at point A is such that $u_r = u_\varphi = 0$ and is thus tangent to a helical line, i.e. $\boldsymbol{u}(\mathrm{A}) = u_B\boldsymbol{e}_B$. Furthermore, if the solution is a quasi-steady equilibrium, then relation $u_H + C = g(\Psi)$ holds and, necessarily, velocity u_H has an extremum at point A because, at point A

$$\partial_\varphi u_H = \frac{\mathrm{d}u_H}{\mathrm{d}\Psi}\partial_\varphi\Psi = 0, \quad \partial_r u_H = \frac{\mathrm{d}u_H}{\mathrm{d}\Psi}\partial_r\Psi = 0. \tag{4.6a,b}$$

Since $\partial_\varphi u_H = r\omega_r$ and $\partial_r u_H = -\omega_\varphi/\alpha$, vorticity at point A is such that $\omega_r = \omega_\varphi = 0$ and is thus tangent to a helical line, i.e. $\boldsymbol{\omega}(\mathrm{A}) = \omega_B\boldsymbol{e}_B$. The points where $\alpha\omega_B$ and u_H reach an extremum generally do not coincide. Only in the particular case when $u_H = 0$, quantity $\alpha\omega_B$ is also a function of Ψ and thus reaches an extremum at the same point. This is illustrated in table 1: for case A with relatively small axial flow, these radial locations differ by less than 0.1 %, while they differ by 3 % for case B because of the larger axial flow.

4.4. *Quasi-equilibrium helical vortex with prescribed parameter values*

The viscous quasi-equilibrium reached after a given simulation time depends on five dimensional parameters used to initiate the simulation as explained in § 4.1, namely circulation Γ, helix radius $r_{A^\star}$, helical pitch $2\pi L$, vortex core size $a^\star$, axial flow intensity $u_H^\star$. The vorticity amplitude $\omega_B^\star$ is a function of circulation Γ and velocity $u_H^\star$. The goal is to generate a quasi-equilibrium to be used as a base flow in an instability study. Hence, we would like to prescribe the final state obtained through the DNS rather than the initial state (4.5*a*,*b*). In order to characterize the final state, we need to define five such parameters. The centre A of the vortex can be determined as explained in the previous section, yielding the helix radius r_A. The helical pitch is a fixed value $2\pi L$ and circulation

https://doi.org/10.1017/jfm.2022.500 Published online by Cambridge University Press

Γ is given by

$$\Gamma \equiv \iint_{\Pi_0} \omega_z \, r \, \mathrm{d}r \, \mathrm{d}\theta. \tag{4.7}$$

The core size can be obtained through an integral in the plane $\Pi_\perp$ associated with point A

$$a^2 \equiv \frac{1}{\Gamma} \iint_{\Pi_\perp} \boldsymbol{\omega} \cdot \boldsymbol{e}_{B_A} \, (\boldsymbol{x} - \boldsymbol{x}_A)^2 \, dS_\perp, \tag{4.8}$$

where $\boldsymbol{e}_{B_A} \equiv \boldsymbol{e}_B(\mathrm{A})$ and $\boldsymbol{x}_A \equiv \boldsymbol{x}(\mathrm{A})$. The last parameter is the axial velocity parameter

$$W_B \equiv \frac{\alpha_A^2}{\pi a^2} \iint_{\Pi_0} u_H \, \mathrm{d}S \quad \text{with } \alpha_A \equiv \alpha(r_A). \tag{4.9}$$

An inverse swirl number can be defined as the ratio of the axial velocity parameter W_B and the typical azimuthal velocity in the core $\Gamma/(2\pi a)$

$$\bar{W}_B \equiv \frac{2\pi a \, W_B}{\Gamma}. \tag{4.10}$$

If the profiles are close to a thin curved Batchelor vortex (4.5*a*,*b*), the core size a is almost equal to $a^\star$ and the quantity W_B is close to the amplitude of helical velocity $\alpha_A u_H^\star$. Indeed, for a thin core, $\mathrm{d}S_\perp \approx \alpha \, \mathrm{d}S \approx \alpha_A \, \mathrm{d}S$ and

$$W_B \approx \frac{\alpha_A}{\pi a^2} \iint_{\Pi_\perp} u_H \mathrm{d}S_\perp = \frac{\alpha_A}{\pi a^2} u_H^\star 2\pi \int_0^\infty \mathrm{e}^{-(\rho/a^\star)^2} \rho \, \mathrm{d}\rho = \frac{\alpha_A}{\pi a^2} u_H^\star \pi a^{\star 2} \approx \alpha_A u_H^\star. \tag{4.11}$$

Another possibility for obtaining a value for a and W_B is to use a Gaussian fit of the axisymmetric component of fields ω_B and/or u_H.

From now on in § 4, all variables are put in dimensionless form using as characteristic dimensional length scale r_A and time scale r_A^2/Γ of the final state. Since the dimensionless radius at point A and dimensionless circulation are equal to one, the quasi-equilibrium state depends only on two dimensionless lengths L and a, and on the inverse swirl number $\bar{W}_B$. In order to simulate the dynamics of the vortex towards the quasi-equilibrium, we also need to select a value for the Reynolds number $Re \equiv \Gamma/(2\pi\nu)$ and a simulation time denoted as T_{sim}. In the two-dimensional framework, it is known that the characteristic time necessary for the vortex to reach a quasi-equilibrium is of order $a^2 Re^{1/3}$ with a pre-factor of order 40 (Bernoff & Lingevitch 1994). We here select the final simulation time $T_{sim} \sim 60 a^2 Re^{1/3}$ and, in practice, check *a posteriori* that it is large enough to reach a quasi-equilibrium. For $Re = 10^4$, for instance, we selected $T_{sim} = 20, 40, 100$ for $a = 0.11, 0.174$ and 0.3, respectively.

The reduced pitch L and circulation Γ of the initial condition are identical to those of the quasi-equilibrium we are looking for (hereafter called the final state). By contrast, initial parameters $r_{A^\star}$, $a^\star$ and $u_H^\star$ differ from the final quantities $r_A = 1$, a and W_B/α_A. We use an iterative procedure to determine these three unknown parameters. First, we select guess values for $a^\star$ and $r_{A^\star}$, so that we link the two initial parameters $u_H^\star$ and $\omega_B^\star$ to parameters a, L and $\bar{W}_B$. This connection is obtained via two 'conservation' laws (B6) and (B12) obtained

https://doi.org/10.1017/jfm.2022.500 Published online by Cambridge University Press

in Appendix B. They read in dimensionless form

$$\mathcal{H}_1(t) - \frac{2}{L}\mathcal{H}_2(t) = 1, \quad \mathcal{H}_4(t) = \mathcal{H}_4(0) - \frac{2t}{L\,Re}, \tag{4.12a,b}$$

where

$$\mathcal{H}_1 \equiv \iint_{\Pi_0} \alpha\omega_B \,\mathrm{d}S, \quad \mathcal{H}_2 \equiv \iint_{\Pi_0} \alpha^4 u_H \,\mathrm{d}S \quad \text{and} \quad \mathcal{H}_4 \equiv \iint_{\Pi_0} u_H \,\mathrm{d}S. \tag{4.13a–c}$$

Let us introduce the quantities

$$I_p^\star(a^\star, r_{A^\star}, L) \equiv \iint_{\Pi_0} \alpha^p \exp(-(\rho/a^\star)^2)\, r\,\mathrm{d}r\,\mathrm{d}\theta, \tag{4.14}$$

with p positive integers. Such quantities depend on L via the quantity ρ, itself depending on $r, \theta, r_{A^\star}$ and L (see figure 1). Inserting the initial condition (4.5*a*,*b*) into (4.12*a*,*b*) allows one to recast variables $\Gamma(t=0)$ and $\mathcal{H}_4(t=T_{sim})$ as

$$\omega_B^\star I_1^\star - \frac{2}{L}u_H^\star I_4^\star = 1, \quad \mathcal{H}_4(T_{sim}) = u_H^\star I_0^\star - \frac{2T_{sim}}{L\,Re}. \tag{4.15a,b}$$

Introducing relation (4.10) leads to determination of $u_H^\star$ and $\omega_B^\star$

$$u_H^\star = \frac{1}{I_0^\star}\left[\frac{\bar{W}_B a}{2\alpha_A^2} + \frac{2T_{sim}}{L\,Re}\right], \quad \omega_B^\star = \frac{1}{I_1^\star}\left(1 + \frac{2}{L}u_H^\star I_4^\star\right). \tag{4.16a,b}$$

Of course, since $a^\star$ and $r_A^\star$ have only been guessed at this stage, the DNS initiated by the above procedure does not lead at once to the prescribed values of a and $r_A = 1$ at $t = T_{sim}$. We have to use a standard iterative procedure to search for the proper pair $(a^\star, r_{A^\star})$ leading, after a simulation time of duration T_{sim}, to the prescribed values $(a, 1)$.

4.5. *Effect of Reynolds number*

The ability to prescribe the final state parameters presented in the previous section makes it possible to use several distinct Reynolds numbers to try to achieve the same quasi-equilibrium state. Figure 8 shows the influence of Re on the two curves $u_H = g(\Psi)$ and $\varpi = f(\Psi)$ obtained numerically. The cases $Re = 5000$ and 10^4 cannot be visually distinguished, yet at lower Reynolds numbers (see $Re = 1000$), the equilibrium curves shift more significantly as the value of Ψ_{max} also decreases. In the following, we always will adopt a sufficiently large Reynolds number (typically $Re = 10^4$) to make sure that the quasi-equilibrium state obtained is Re-independent.

4.6. *Helical vortex cases*

Using the procedure presented, we generate several base flow configurations with various values of parameters L, a and $\bar{W}_B$. For a helical vortex of reduced pitch L, curvature is given by $\kappa = 1/(1+L^2)$ and torsion by $\tau = L/(1+L^2)$. As plotted in figure 9, curvature κ decreases from 1 to 0 as L increases from 0, while torsion τ first increases from 0 to 0.5 (reached for $L = 1$), and then slowly decreases to 0. The asymptotic theory presented in § 5.1 uses parameter $\varepsilon \equiv a\kappa$ as a small parameter to introduce curvature effects on a straight axisymmetric vortex. A given value of ε can be achieved from different pair values (L, a), thus corresponding to different curvature and torsion levels. We choose five helical vortex states, the parameters of which are presented in table 2.

https://doi.org/10.1017/jfm.2022.500 Published online by Cambridge University Press

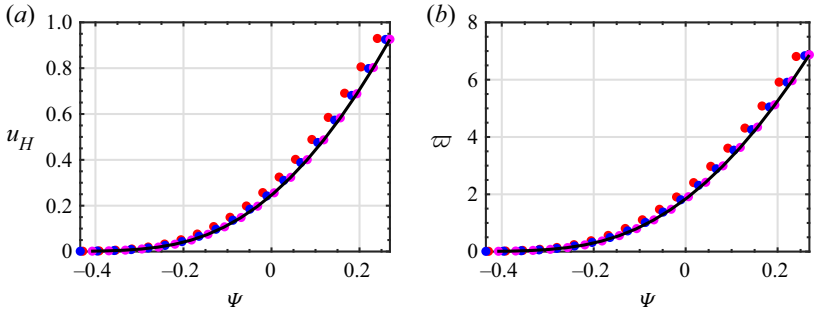

Figure 8. Relations (*a*) $u_H = g(\Psi)$ and (*b*) $\varpi = f(\Psi)$ for quasi-equilibria obtained at different Reynolds numbers: $Re = 500$ (red dots, $T_{sim} = 4$), $Re = 10^3$ (blue dots, $T_{sim} = 4$), $Re = 5 \times 10^3$ (magenta dots, $T_{sim} = 10$) and $Re = 10^4$ (black solid line, $T_{sim} = 20$). The dimensionless parameters of these states are $L = 0.3$, $a = 0.11$ and $\bar{W}_B = 0.2$.

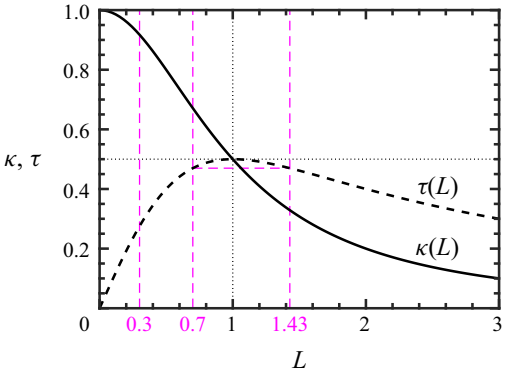

Figure 9. Non-dimensional curvature κ (solid line) and torsion τ (black dashed line) as functions of the reduced pitch L. Pitches L and $1/L$ lead to the same value of the torsion but to different curvature levels, as illustrated for $L = 0.7$ and $1/0.7 \approx 1.43$.

Case	$\bar{W}_B$	L	a	ε	κ	τ
BS1	0.2	0.3	0.11	0.1	0.92	0.28
BS2	0.2	1.43	0.3	0.1	0.33	0.47
BS3	0.4	0.3	0.11	0.1	0.92	0.28
BS4	0.4	0.3	0.174	0.16	0.92	0.28
BS5	−0.4	0.3	0.174	0.16	0.92	0.28

Table 2. Parameters ($\bar{W}_B, L, a$) of the DNS cases investigated, with corresponding values of parameter ε, curvature κ and torsion τ.

The first three states correspond to the same value of $\varepsilon = 0.1$ but to different geometrical parameter values. State BS1 is characterized by relatively small values of the helical pitch and core size, leading to high curvature and low torsion. State BS2 is characterized by larger values of the helical pitch and core size, leading to low curvature but near-maximum torsion. State BS3 is the same as BS1 except that the inverse swirl parameter $\bar{W}_B$ is twice as much that of BS1 (or BS2). State BS4 is a state with a larger value $\varepsilon = 0.16$ obtained

https://doi.org/10.1017/jfm.2022.500 Published online by Cambridge University Press

through a larger core size. State BS5 is similar to BS4, yet with reversed axial flow (hence negative inverse swirl).

5. Core structure: asymptotic theory and DNS results

The asymptotic theory initially developed by Blanco-Rodríguez *et al.* (2015) considers a straight Batchelor vortex as reference state, which is assumed to be strained via local and global effects. We start again this section using dimensional variables and suppose that there exists a frame of reference in which the helical vortex is steady. In that frame, the helical vortex is located around a centre line $\boldsymbol{x}_0(\theta_s) = r_A \boldsymbol{e}_r(\theta_s) + L\theta_s \boldsymbol{e}_z$ where θ_s is a continuous parameter, with associated tangent vector

$$\boldsymbol{e}_b \equiv \boldsymbol{e}_{B_A} = \alpha_A \left[\frac{r_A}{L} \boldsymbol{e}_\theta(\theta_s) + \boldsymbol{e}_z \right]. \tag{5.1}$$

For a helical vortex filament, the distribution around the centreline in the plane $\Pi_\perp(\mathrm{A})$ is characterized by a circulation Γ and a core size a. At a given point on a helical vortex, local effects are curvature and torsion, and global ones are due to the remote vorticity of nearby helix turns. Under the limitation of small core size a with respect to r_A and L, the vortex is close to a straight cylinder, with its local cylindrical basis $(\boldsymbol{e}_\rho, \boldsymbol{e}_\psi, \boldsymbol{e}_b)$. Curvature effects are introduced as small amplitude perturbations to the reference axisymmetric state via a small self-strain parameter

$$\varepsilon = \alpha_A^2 \frac{r_A}{L} \frac{a}{L} = \kappa a \ll 1, \tag{5.2}$$

which can then be used to expand the velocity field in power series. The theory is valid is the limit of small core sizes ($a \ll r_A$ and $a \ll L$), which implies $\varepsilon \ll 1$. It has been shown in Callegari & Ting (1978) and Blanco-Rodríguez & Le Dizès (2016, 2017) that the dominant deformation stems from local curvature, and sets in as a dipolar first-order term in ε. Local torsion and remote vorticity effects only appear at second order. We focus here on first-order effects and characterize how local curvature deforms the vortex core.

Since the reference state is a straight Batchelor vortex, we adopt, from now on in this section, the core size a as characteristic size and $\Gamma/(2\pi a)$ as characteristic velocity, and denote dimensionless quantities with a bar, for instance $\bar{\rho} = \rho/a$ stands for the non-dimensional radial distance to point A in the plane $\Pi_\perp$. We use cylindrical coordinates $(\bar{\rho}, \psi, b)$, where b denotes the component parallel to the vortex axis. As mentioned above, the velocity field $\bar{\boldsymbol{u}} = (\bar{u}_\rho, \bar{u}_\psi, \bar{u}_b)$ can be expanded in power series in ε

$$\bar{\boldsymbol{u}}(\bar{\rho}, \psi) = (\varepsilon \bar{u}_\rho^{(1)} + \cdots)\, \boldsymbol{e}_\rho + (\bar{u}_\psi^{(0)} + \varepsilon \bar{u}_\psi^{(1)} + \cdots)\, \boldsymbol{e}_\psi + (\bar{u}_b^{(0)} + \varepsilon u_b^{(1)} + \cdots)\, \boldsymbol{e}_b, \tag{5.3}$$

with a similar expansion for vorticity.

5.1. *Asymptotic expansion*

The leading-order term $\bar{\boldsymbol{u}}^{(0)}$ is assumed to be a Batchelor vortex. Indeed, this vortex model is known to be a self-similar attracting viscous solution for two-dimensional vortices with axial flow. Such a profile is also found experimentally and numerically in the core of helical vortices (Ali & Abid 2014; Selçuk *et al.* 2017; Okulov *et al.* 2019; Shtork *et al.* 2020).

https://doi.org/10.1017/jfm.2022.500 Published online by Cambridge University Press

This means that the velocity distribution in the plane $\Pi_\perp$ is

$$\bar{u}_\rho^{(0)} = 0, \quad \bar{u}_\psi^{(0)} = \frac{1-\exp(-\bar{\rho}^2)}{\bar{\rho}}, \quad \bar{u}_b^{(0)} = \bar{W}_0 \exp(-\bar{\rho}^2) + \bar{W}_{00}. \tag{5.4a–c}$$

The parameter $\bar{W}_0$ indicates the jet strength in the axial direction and the parameter $\bar{W}_{00}$ is a correction at leading order deduced from the background velocity outside the vortex. Based on these velocity fields, the vorticity field at zeroth order in ε is

$$\bar{\boldsymbol{\omega}}^{(0)} = \bar{\omega_B}^{(0)} \boldsymbol{e}_b + \bar{\omega}_\psi^{(0)} \boldsymbol{e}_\psi, \tag{5.5}$$

with

$$\bar{\omega_B}^{(0)} = 2\exp(-\bar{\rho}^2), \quad \bar{\omega}_\psi^{(0)} = 2\bar{W}_0 \bar{\rho} \exp(-\bar{\rho}^2). \tag{5.6a,b}$$

For any point M in plane $\Pi_\perp$(A) except A itself, the velocity component u_B along direction $\boldsymbol{e}_B$(M) is different from the velocity component u_b along the direction $\boldsymbol{e}_b \equiv \boldsymbol{e}_B$(A) orthogonal to the plane. Quantity u_B/α is given by

$$\frac{u_B}{\alpha} = \frac{u_\rho}{\alpha}\, \boldsymbol{e}_\rho \cdot \boldsymbol{e}_B + \frac{u_\psi}{\alpha}\, \boldsymbol{e}_\psi \cdot \boldsymbol{e}_B + \frac{u_b}{\alpha}\, \boldsymbol{e}_b \cdot \boldsymbol{e}_B, \tag{5.7}$$

where $\alpha \equiv \alpha$(M). Using relations (deduced from relations (C3)–(C11) in Appendix C)

$$\boldsymbol{e}_\rho \cdot \boldsymbol{e}_B = 0, \quad \boldsymbol{e}_\psi \cdot \boldsymbol{e}_B = \alpha\alpha_A \frac{\rho}{L}, \quad \boldsymbol{e}_b \cdot \boldsymbol{e}_B = \alpha\alpha_A \left(1 + \frac{r_A^2}{L^2} - \frac{r_A}{L}\frac{\rho}{L}\cos\psi\right), \tag{5.8a–c}$$

one obtains, at zeroth order in ε

$$\frac{\bar{u}_B^{(0)}}{\alpha} = \frac{\bar{u}_b^{(0)}(\bar{\rho})}{\alpha_A} + \bar{u}_\psi^{(0)}(\bar{\rho})\alpha_A \frac{\bar{\rho}}{\bar{L}} = \frac{1}{\alpha_A}[\bar{W}_0 \exp(-\bar{\rho}^2) + \bar{W}_{00}] + \frac{\alpha_A}{\bar{L}}[1 - \exp(-\bar{\rho}^2)]. \tag{5.9}$$

Quantity $\bar{W}_0$ is, by construction, given by $\bar{W}_0 = \bar{u}_b^{(0)}(0) - \bar{u}_b^{(0)}(\infty)$. Using relation (5.9) twice at $\bar{\rho} = 0$ and at the limit $\bar{\rho} \to \infty$, one deduces, at zeroth order in ε

$$\bar{W}_0 = \alpha_A \left(\frac{\bar{u}_B^{(0)}(0)}{\alpha_A} - \frac{\bar{u}_B^{(0)}(\infty)}{\alpha}\right) + \frac{\alpha_A^2}{\bar{L}} = \alpha_A \bar{u}_H^{(0)}(0) + \frac{\alpha_A^2}{\bar{L}}. \tag{5.10}$$

Quantity $\bar{W}_{00}$ can be obtained by matching the value reached by $\bar{u}_B^{(0)}/\alpha$ outside the vortex to the constant introduced in (3.10)

$$\bar{C} = \frac{2\pi a C}{\Gamma} = \frac{1}{\bar{L}} + \bar{U}_z^{\infty(T)}. \tag{5.11}$$

As $\bar{\rho} \to \infty$, expression (5.9) tends to $\bar{W}_{00}/\alpha_A + \alpha_A/\bar{L}$. The matching eventually yields

$$\bar{W}_{00} = \alpha_A \left(\bar{C} - \frac{\alpha_A}{\bar{L}}\right) = \alpha_A \bar{U}_z^{\infty(T)} + \frac{\alpha_A(1-\alpha_A)}{\bar{L}}. \tag{5.12}$$

In Blanco-Rodríguez *et al.* (2015), the simplified expression $\bar{W}_{00} \approx \alpha_A U_z^{\infty(T)}$ was used. Expression (5.12) shows a better agreement with the numerical results (see § 5.2).

https://doi.org/10.1017/jfm.2022.500 Published online by Cambridge University Press

The two constants $\bar{W}_0$ and $\bar{W}_{00}$ can thus be related to the parameter values of the base helical vortex using (5.10) and (5.12) with $\bar{U}_z^{\infty(T)} = -\bar{U}_0 = \bar{\Omega}_0\bar{L}$

$$\bar{W}_0 \approx \bar{W}_B + \frac{\alpha_A^2}{\bar{L}}, \quad \bar{W}_{00} = \alpha_A\bar{\Omega}_0\bar{L} + \frac{\alpha_A(1-\alpha_A)}{\bar{L}}. \tag{5.13a,b}$$

The evaluation of $\bar{W}_{00}$ requires the knowledge of $\bar{\Omega}_0$. Although this latter quantity could be computed theoretically (Okulov 2004) as done by Brynjell-Rahkola & Henningson (2020), we use here the value deduced from the DNS results.

Going now to order ε, the perturbation is purely dipolar (Blanco-Rodríguez *et al.* 2015)

$$\bar{u}_\rho^{(1)} = -\frac{\bar{\Psi}^{(1)}}{\bar{\rho}}\sin\psi, \quad \bar{u}_\psi^{(1)} = \left[\bar{\rho}\bar{u}_\psi^{(0)} - \frac{\mathrm{d}\bar{\Psi}^{(1)}}{\mathrm{d}\bar{\rho}}\right]\cos\psi, \tag{5.14a,b}$$

$$\bar{u}_b^{(1)} = \left[\bar{\rho}\bar{u}_b^{(0)} - \frac{1}{\bar{u}_\psi^{(0)}}\frac{\mathrm{d}\bar{u}_b^{(0)}}{\mathrm{d}\bar{\rho}}\bar{\Psi}^{(1)}\right]\cos\psi, \tag{5.15}$$

where the first-order streamfunction perturbation $\bar{\Psi}^{(1)}(\bar{\rho})$ satisfies

$$\bar{\Psi}^{(1)} = \bar{\Psi}_0^{(1)} + \bar{W}_0^2\bar{\Psi}_1^{(1)} + \bar{W}_{00}\bar{W}_0\bar{\Psi}_2^{(1)}. \tag{5.16}$$

The three contributions $\bar{\Psi}_0^{(1)}$, $\bar{\Psi}_1^{(1)}$ and $\bar{\Psi}_2^{(1)}$ are solutions of

$$\mathcal{L}\bar{\Psi}_0^{(1)} = \bar{K}_0, \quad \mathcal{L}\bar{\Psi}_1^{(1)} = \bar{K}_1, \quad \mathcal{L}\bar{\Psi}_2^{(1)} = \bar{K}_2, \tag{5.17a–c}$$

where the linear operator $\mathcal{L}(\bullet)$ is defined as

$$\mathcal{L}(\bullet) \equiv \frac{\partial^2(\bullet)}{\partial\bar{\rho}^2} + \frac{1}{\bar{\rho}}\frac{\partial(\bullet)}{\partial\bar{\rho}} - \left(\frac{1}{\bar{\rho}^2} + H_0(\bar{\rho})\right)(\bullet) \tag{5.18}$$

and

$$\left.\begin{aligned}
&\bar{H}_0(\bar{\rho}) \equiv \frac{1}{\bar{u}_\psi^{(0)}}\frac{\mathrm{d}\bar{\omega}_B{}^{(0)}}{\mathrm{d}\bar{\rho}} = \frac{-4\bar{\rho}^2}{\exp(\bar{\rho}^2)-1},\\
&\bar{K}_0(\bar{\rho}) \equiv 2\bar{\rho}\bar{\omega}_b^{(0)} + \bar{u}_\psi^{(0)} = \frac{1-\exp(-\bar{\rho}^2)}{\bar{\rho}} + 4\bar{\rho}\exp(-\bar{\rho}^2),\\
&\bar{K}_1(\bar{\rho}) \equiv -\frac{4\bar{\rho}^3}{\exp(\bar{\rho}^2)-1}\exp(-\bar{\rho}^2), \quad \bar{K}_2(\bar{\rho}) \equiv -\frac{4\bar{\rho}^3}{\exp(\bar{\rho}^2)-1}.
\end{aligned}\right\} \tag{5.19}$$

The boundary conditions at $\bar{\rho} = 0$ are

$$\bar{\Psi}_i^{(1)}(0) = 0, \quad \frac{\partial\bar{\Psi}_i^{(1)}}{\partial\bar{\rho}}(0) = 0, \quad i = 0, 1, 2. \tag{5.20}$$

We hence compute the first-order streamfunction perturbation $\bar{\Psi}^{(1)}$ numerically. For large $\bar{\rho}$, $\bar{\Psi}^{(1)}(\rho)$ expands as (Fukumoto & Miyazaki 1991)

$$\bar{\Psi}^{(1)}(\bar{\rho}) \sim \frac{1}{2}\bar{\rho}\log\bar{\rho} + \bar{\rho}\bar{A} + O\left(\frac{1}{\bar{\rho}}\right), \tag{5.21}$$

https://doi.org/10.1017/jfm.2022.500 Published online by Cambridge University Press

where, for the Batchelor vortex profile, $\bar{A}$ reads as

$$\bar{A} = \frac{1}{4}[1 - \bar{W}_0(\bar{W}_0 + 4\bar{W}_{00}) + \gamma - \log 2], \quad \gamma \approx 0.577. \tag{5.22}$$

This formula corrects the typo $2\bar{W}_{00}$ in (3.12) of Blanco-Rodríguez *et al.* (2015).

5.2. *Comparison with DNS results*

Quasi-equilibrium states listed in table 2 are obtained as final states of simulations through the procedure explained in § 4.4. Figure 10(*a*) (respectively figure 10*b*) shows the axial vorticity in the plane $\Pi_\perp$ for BS1 (respectively BS2). In addition, the internal structure can be compared with the results obtained by the asymptotic theory presented in § 5.1. To do so, one needs not only to rewrite the DNS results in the reference frame and in the basis used in the theory, but also to use the same non-dimensionalization process. More precisely, this means:

(i) adopting the frame (T) translating at velocity $U_0\boldsymbol{e}_z$ with the vortex. This amounts to transforming two of the velocity components: $u_B \longrightarrow u_B - \alpha U_0$ and $u_\varphi \longrightarrow u_\varphi + \alpha U_0 r/L$;

(ii) projecting the velocity field onto the plane $\Pi_\perp$(A) in order to get in-plane components (u_ρ, u_ψ) and deduce out-of-plane component u_b, as explained in Appendix C;

(iii) performing an azimuthal decomposition in $\Pi_\perp$(A) of such components using

$$u^{(m)}_{\rho,\psi,b}(\rho_i) = \frac{1}{N_\psi}\sum_{j=1}^{N_\psi} u_{\rho,\psi,b}(\rho_i, \psi_j)\mathrm{e}^{-\mathrm{i}m\psi_j} \quad (i = 1, \ldots, N_\rho), \tag{5.23}$$

where (ρ_i, ψ_j) are the locations of $N_\rho \times N_\psi$ nodes of a polar mesh in plane $\Pi_\perp$; and

(iv) making the various quantities dimensionless using the reference scales a_0 and $2\pi a_0^2/\Gamma$ as for the theory.

Based on the above procedure, the parameters presented in table 2 correspond to the values of effective core size a_0, inverse swirl $\bar{W}_0$ and constant $\bar{W}_{00}$ reported in table 3. Each case has been analysed, showing the adequacy of the asymptotic theory up to relatively large values of ε. Comparisons between asymptotic theory and DNS of helical vortices are shown in figures 11 and 12 for BS1 ($\varepsilon = 0.1$) and BS5 ($\varepsilon = 0.16$), respectively. In each graph, the $m = 0$ and $m = 1$ contributions to $(u_\rho^{(m)}, u_\psi^{(m)}, u_b^{(m)})$ are plotted. Excellent agreement is found for the axisymmetric part. A fairly small mismatch subsists for the components of the $m = 1$ contribution.

6. Discussion and conclusion

In this paper, we have shown that, when a moderate axial flow is present in a helical vortex, a quasi-equilibrium can be reached. In a suitable translating frame (T), such a solution can be related to a broader family of equilibria of inviscid flows characterized by a helical symmetry of pitch $2\pi L$. We have first exhibited the constraints (3.15*a*,*b*) of such equilibria, which involve the velocity and vorticity components $u_B^{(T)}$ and ω_B: introducing a streamfunction $\Psi^{(T)}$ defined by (2.1), there exist two functions f and g such that $\varpi = f(\Psi^{(T)})$ and $u_B^{(T)}/\alpha = g(\Psi^{(T)})$, where ϖ is defined in (3.14). Such relationships,

https://doi.org/10.1017/jfm.2022.500 Published online by Cambridge University Press

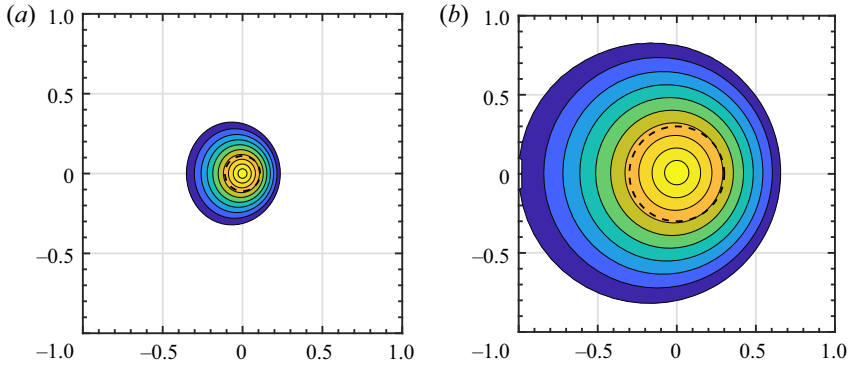

Figure 10. (*a*) Contours of ω_B in plane $\Pi_\perp$ for the quasi-equilibrium state BS1. (*b*) Same for BS2, with the same spatial range represented. Contour levels are as in figure 2. The Reynolds number is $Re = 10^4$, and the simulation time $T_{sim} = 20$ (respectively 100) for BS1 (respectively BS2).

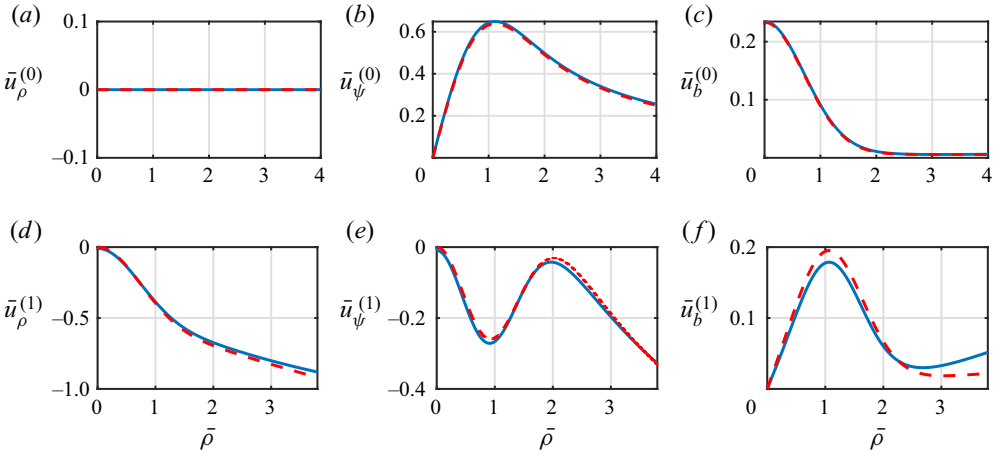

Figure 11. Case BS1: radial distributions of velocity components $(\bar{u}_\rho^{(m)}, \bar{u}_\psi^{(m)}, \bar{u}_b^{(m)})$ for $m = 0$ (*a–c*) and $m = 1$ (*d–f*). Blue solid line: DNS results; red dashed line: theory.

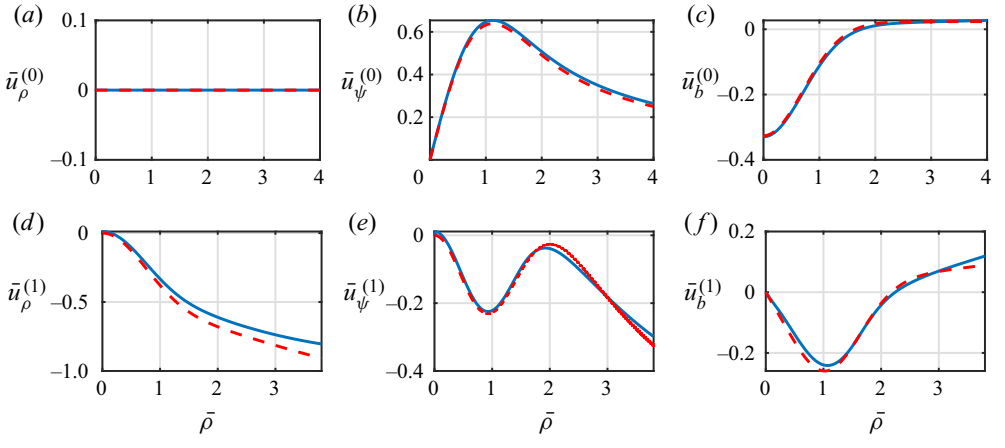

Figure 12. Same as figure 11 for case BS5.

https://doi.org/10.1017/jfm.2022.500 Published online by Cambridge University Press

	Case parameters		DNS results		Theory (5.13*a*,*b*)	
Case	a	$\bar{W}_B$	a_0	$\bar{W}_0$	$\bar{W}_B + \alpha_A^2/\bar{L}$	$\bar{W}_{00}$
BS1	0.11	0.2	0.1108	0.2293	0.23	0.0059
BS2	0.3	0.2	0.3001	0.3421	0.341	−0.1108
BS3	0.11	0.4	0.1109	0.4271	0.43	0.0069
BS4	0.174	0.4	0.1767	0.4419	0.448	0.0255
BS5	0.174	−0.4	0.1731	−0.3524	−0.352	0.0238

Table 3. For the different helical vortex states under study: case parameters a and $\bar{W}_B$; effective core size a_0 and inverse swirl $\bar{W}_0$ obtained by DNS; values of $\bar{W}_B + \alpha_A^2/\bar{L}$ and $\bar{W}_{00}$ obtained through (5.13*a*,*b*).

which extend formulae known for vortex rings, are indeed reached in time through DNS when a single helical vortex with an axial flow relaxes towards quasi-equilibrium. We also describe a numerical procedure aimed at computing vortex solutions with all parameters prescribed, namely circulation, helix radius, helical pitch, vortex core size and swirl level. The procedure is first used to show that such quasi-equilibria do not depend on the Reynolds number used to generate them, if sufficiently large. More generally they can be used as basic flow profiles for the purpose of instability studies, and several helical vortex states are described (see parameters in table 2). Finally, when the core size is reasonably small with respect to the helical pitch and the curvature radius, the asymptotic theory is shown to adequately describe the structure of the DNS velocity field. At zeroth order (local axisymmetric contribution), the flow is found to be very close to a straight Batchelor vortex flow profile, a property that is used to compute the dipolar correction at first order due to the curvature of the vortex; excellent agreement is found between numerics and asymptotic theory.

The procedure used above relies on the assumption that the initial condition rapidly relaxes towards a quasi-equilibrium. However, when the axial flow becomes large, such an equilibrium ceases to exist because the swirling motion can no longer counter-balance the centrifugal forces generated by axial velocity in the curved vortex. In terms of vorticity, negative helical vorticity emerges and may persist over large evolution times. We can define a threshold value $\bar{W}_B^c$ above which negative vorticity is still present at $t = T_{sim}$ (here $T_{sim} = 4$ at $Re = 10^3$). In figure 13, we present the evolution of this threshold $\bar{W}_B^c$ as a function of the reduced pitch at fixed core size $a = 0.11$. For given L and $\bar{W}_B < \bar{W}_B^c(L)$, the simulation converges towards a quasi-equilibrium state as shown in figure 14(*a–d*). For $\bar{W}_B > \bar{W}_B^c(L)$, the system does not rapidly reach such an equilibrium (figure 14*e–h*). A dipolar structure can even emerge, as illustrated in figure 15. This phenomenon is similar to what is observed in vortex rings by Cheng, Lou & Lim (2010) when the axial flow becomes significant. Note also that the threshold value shown in figure 13 pinpoints the existence of an equilibrium up to relatively large values of $\bar{W}_B$. However, we suspect this helical equilibrium state to be itself unstable with respect to the swirling jet instability that occurs as soon as $\bar{W}_B > 0.7$ for a straight Batchelor vortex (Lessen *et al.* 1974; Mayer & Powell 1992). In our simulations, enforcing the helical symmetry filters out such instabilities.

In the present paper, the method and the data are presented in the case of a single helical vortex. This could be easily extended to an arbitrary number of vortices with the same helical pitch in a quasi-equilibrium arrangement. These states are of great significance for the instability studies of vortices with a helical shape, e.g. in the wake of wind turbines, marine propellers, helicopter rotors.... Let us stress the importance of monitoring the

https://doi.org/10.1017/jfm.2022.500 Published online by Cambridge University Press

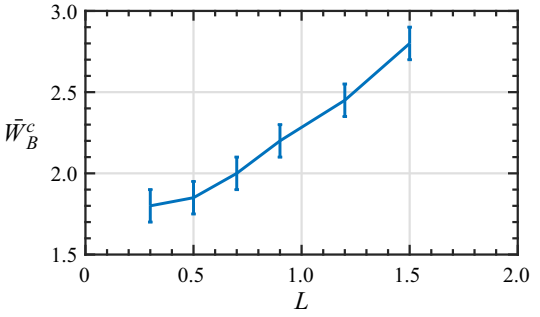

Figure 13. Axial flow critical level $\bar{W}_B^c(L)$ above which the initial condition does not relax towards a quasi-steady equilibrium. Simulations with $a = 0.11$, $Re = 10^3$ and $T_{sim} = 4$.

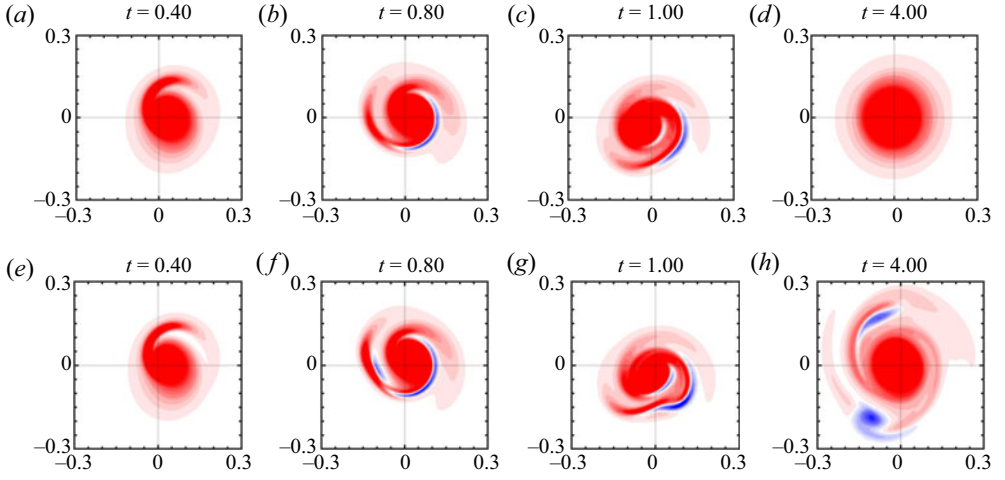

Figure 14. Time evolution of a helical vortex at $L = 0.3$, $a = 0.11$ and $Re = 10^3$ with axial flow (*a–d*) $\bar{W}_B = 1.8$ (below the critical threshold) and (*e–h*) $\bar{W}_B = 1.9$ (above it). Contours of $\omega_b/\omega_{b\,max}$ in plane $\Pi_\perp(t)$. Contour levels are regularly spaced in the range $[-1/e, 1/e]$ (from blue to red).

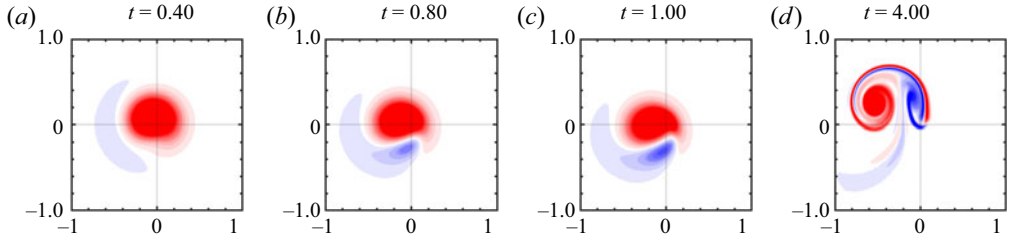

Figure 15. Time evolution of a helical vortex at $L = 1.43$, $a = 0.3$ and $Re = 10^3$ with axial flow $\bar{W}_B = 4.0$ (above the threshold). Contours are as in figure 14.

axial velocity in such vortices, since curvature and elliptic short-wave instabilities crucially depend on the swirl parameter (Hattori & Fukumoto 2014). In this perspective, the present work provides a procedure to generate basic states with prescribed values of the numerous parameters characterizing the helical vortex, namely circulation, helix radius, helical pitch, vortex core size and swirl level.

https://doi.org/10.1017/jfm.2022.500 Published online by Cambridge University Press

Acknowledgements. The authors would like to thank Y. Hattori for fruitful discussions.

Declaration of interests. The authors report no conflict of interest.

Author ORCIDs.
Yonghui Xu https://orcid.org/0000-0001-5779-3505;
Ivan Delbende https://orcid.org/0000-0003-0000-0070;
Maurice Rossi https://orcid.org/0000-0002-4762-1248.

Appendix A. Estimating quantity $\mathrm{d}u_H/\mathrm{d}\Psi$

The second condition of (3.15*a*,*b*) requires the derivative $\mathrm{d}u_H/\mathrm{d}\Psi$. This quantity is *a priori* defined only if a steady state is reached. The following procedure, however, allows us to estimate this quantity during the whole time evolution, based on averages and least square interpolation. More specifically, we discretize the Ψ-axis in N_Ψ intervals of length $\Delta\Psi$ between the minimum and the maximum value of Ψ. In each interval $[\Psi_i - \Delta\Psi/2, \Psi_i + \Delta\Psi/2]$, there is a certain number K_i of points $(\Psi^{(k)}, u_H^{(k)})$ indexed by k. The mean value α_i of $u_H^{(k)}$ and the estimate β_i of $\mathrm{d}u_H/\mathrm{d}\Psi$ at point Ψ_i are such that

$$K_i\alpha_i + \beta_i \sum_k (\Psi^{(k)} - \Psi_i) = \sum_k u_H^{(k)}, \tag{A1}$$

$$\alpha_i \sum_k (\Psi^{(k)} - \Psi_i) + \beta_i \sum_k (\Psi^{(k)} - \Psi_i)^2 = \sum_k [u_H^{(k)}(\Psi^{(k)} - \Psi_i)], \tag{A2}$$

where it has been assumed that $u_H^{(k)}$ can be estimated with the linear interpolation

$$u_H^{(k)} = \alpha_i + \beta_i(\Psi^{(k)} - \Psi_i). \tag{A3}$$

Quantities $\mathrm{d}u_H/\mathrm{d}\Psi$ are computed using a linear interpolation along the variable Ψ as follows:

$$\frac{\mathrm{d}u_H}{\mathrm{d}\Psi_T}(\Psi^{(k)}) = \beta_i + \begin{Bmatrix} \beta_{i+1} - \beta_i \\ \beta_i - \beta_{i-1} \end{Bmatrix} \frac{\Psi^{(k)} - \Psi_i}{\Delta\Psi} \quad \begin{Bmatrix} \text{if } \Psi^{(k)} > \Psi_i \\ \text{if } \Psi^{(k)} < \Psi_i \end{Bmatrix}. \tag{A4}$$

For the first and the last half-intervals, one uses an extrapolation from the neighbouring half-interval.

Appendix B. Relations for some global quantities in viscous helical flows

In this appendix, quantities are dimensional. For a viscous flow of specific volume υ periodic along z of period $2\pi L$ and characterized by a compact vorticity field, the circulation Γ and the axial momentum per unit length $\mathcal{P}_z$ given by

$$\Gamma = \iint_{\Pi_0} \omega_z\, r\, \mathrm{d}r\, \mathrm{d}\theta, \quad \mathcal{P}_z = \frac{1}{2\pi L}\left(\frac{1}{2\upsilon}\iiint_V \boldsymbol{x}\times\boldsymbol{\omega}\,\mathrm{d}V\right)\cdot\boldsymbol{e}_z = \frac{1}{4\pi L\upsilon}\iiint_V r\omega_\theta\,\mathrm{d}V, \tag{B1a,b}$$

are two global viscous invariants. In (B1*a*,*b*), Π_0 denotes the plane $z = 0$ and V the volume defined by $z \in [-\pi L, \pi L]$. For such periodic flows, the axial angular momentum per

https://doi.org/10.1017/jfm.2022.500 Published online by Cambridge University Press

unit length

$$\mathcal{L}_z = -\frac{1}{4\pi L\upsilon}\iiint_V \boldsymbol{x}^2\omega_z \,\mathrm{d}V \tag{B2}$$

is not an invariant but evolves according to

$$\frac{\mathrm{d}\mathcal{L}_z}{\mathrm{d}t} = -2\mu\Gamma, \tag{B3}$$

where $\mu \equiv \nu/\upsilon$.

These conservation laws applied to viscous helical flows (Selçuk *et al.* 2017) provide relations between the following unsteady quantities:

$$\mathcal{H}_1 \equiv \iint_{\Pi_0} \alpha\omega_B \,\mathrm{d}S, \quad \mathcal{H}_2 \equiv \iint_{\Pi_0} \alpha^4 u_H \,\mathrm{d}S, \quad \mathcal{H}_3 \equiv \iint_{\Pi_0} r^2\alpha\omega_B \,\mathrm{d}S, \quad \mathcal{H}_4 \equiv \iint_{\Pi_0} u_H \,\mathrm{d}S. \tag{B4a–d}$$

Since $\omega_z = \alpha(\omega_B - r\omega_\varphi/L)$ for helical flows, the conservation circulation Γ yields

$$\Gamma = \iint_{\Pi_0} \alpha\omega_B \,\mathrm{d}S + \iint_{\Pi_0} \frac{\alpha^2 r}{L}\frac{\partial u_H}{\partial r}\,\mathrm{d}S. \tag{B5}$$

Integrating by parts the last integral leads to

$$\Gamma = \mathcal{H}_1(t) - \frac{2}{L}\mathcal{H}_2(t). \tag{B6}$$

Similarly, the conservation of axial momentum per unit length $\mathcal{P}_z$, implies for helical flows that

$$\mathcal{P}_z = \frac{1}{4\pi L\upsilon}\int_{-\pi L}^{\pi L}\left[\iint_{\Pi_0} r\omega_\theta \, r\,\mathrm{d}r\,\mathrm{d}\theta\right]\mathrm{d}z = \frac{1}{2\upsilon}\iint_{\Pi_0} r^2\omega_\theta \,\mathrm{d}r\,\mathrm{d}\theta. \tag{B7}$$

Introducing $\omega_\theta = \alpha(\omega_\varphi + (r/L)\omega_B)$ and integrating by parts, yields

$$\mathcal{P}_z\upsilon = \frac{1}{2L}\mathcal{H}_3(t) + \mathcal{H}_2(t). \tag{B8}$$

Finally, helical symmetry imposes

$$\iiint_V \boldsymbol{x}^2\omega_z \,\mathrm{d}V = \iiint_V (z^2 + r^2)\omega_z \,\mathrm{d}V = \frac{2\Gamma(\pi L)^3}{3} + 2\pi L\iint_{\Pi_0} r^2\omega_z \,\mathrm{d}S. \tag{B9}$$

Upon introducing $\omega_z = \alpha(\omega_B - r\omega_\varphi/L)$, one gets

$$\begin{aligned}\iint_{\Pi_0} r^2\omega_z \,\mathrm{d}S &= \iint_{\Pi_0} \alpha r^2\omega_B \,\mathrm{d}S + \iint_{\Pi_0} \frac{\alpha^2 r^3}{L}\frac{\partial u_H}{\partial r}\,\mathrm{d}S \\ &= \mathcal{H}_3(t) + \iint_{\Pi_0} rL(1-\alpha^2)\frac{\partial u_H}{\partial r}\,\mathrm{d}S.\end{aligned} \tag{B10}$$

Integrating by parts the last integral yields

$$\mathcal{L}_z(t) = -\frac{1}{4\pi L\upsilon}\iiint_V \boldsymbol{x}^2\omega_z \,\mathrm{d}V = -\frac{\Gamma(\pi L)^2}{6\upsilon} - L\mathcal{P}_z + \frac{L}{\upsilon}\mathcal{H}_4(t). \tag{B11}$$

Since circulation Γ and axial momentum per unit length $\mathcal{P}_z$ are global viscous invariants for a compact vorticity field and that the axial angular momentum per unit length $\mathcal{L}_z(t)$ evolves according to (B3), one gets

$$\frac{\mathrm{d}\mathcal{H}_4}{\mathrm{d}t} = -\frac{2\Gamma}{L}\nu \quad \text{or equivalently} \quad \mathcal{H}_4(t) = \mathcal{H}_4(0) - \frac{2\Gamma}{L}\nu t. \tag{B12}$$

https://doi.org/10.1017/jfm.2022.500 Published online by Cambridge University Press

Appendix C. Projection of the velocity field on the $\Pi_\perp$ plane

Point A denotes the vortex centre, with the associated Serret–Frenet basis $(\boldsymbol{e}_{r_A}, \boldsymbol{e}_{\varphi_A}, \boldsymbol{e}_{B_A})$ such that

$$\boldsymbol{e}_{\varphi_A}(r_A, \theta_A) = \alpha_A \left(\boldsymbol{e}_{\theta_A} - \frac{r_A}{L} \boldsymbol{e}_z \right), \tag{C1}$$

$$\boldsymbol{e}_{B_A}(r_A, \theta_A) = \alpha_A \left(\frac{r_A}{L} \boldsymbol{e}_{\theta_A} + \boldsymbol{e}_z \right), \tag{C2}$$

where $\alpha_A = (1 + r_A^2/L^2)^{-1/2}$ (see figure 1 for a similar geometry). The plane $\Pi_\perp$ is spanned by the Cartesian basis $(\boldsymbol{e}_{r_A}, \boldsymbol{e}_{\varphi_A})$, with which a local polar basis $(\boldsymbol{e}_\rho, \boldsymbol{e}_\psi)$ is associated

$$\boldsymbol{e}_\rho = \cos\psi\, \boldsymbol{e}_{r_A} + \sin\psi\, \boldsymbol{e}_{\varphi_A}, \tag{C3}$$

$$\boldsymbol{e}_\psi = -\sin\psi \boldsymbol{e}_{r_A} + \cos\psi\, \boldsymbol{e}_{\varphi_A}, \tag{C4}$$

and a normal vector to the plane is $\boldsymbol{e}_b \equiv \boldsymbol{e}_{B_A}$. The velocity field at any point M_0 in plane Π_0 is given by

$$\boldsymbol{u}(\mathrm{M}_0) = u_r(\mathrm{M}_0)\boldsymbol{e}_r(\mathrm{M}_0) + u_\varphi(\mathrm{M}_0)\boldsymbol{e}_\varphi(\mathrm{M}_0) + u_B(\mathrm{M}_0)\boldsymbol{e}_B(\mathrm{M}_0). \tag{C5}$$

In order to express the velocity field in plane $\Pi^\perp$ using the basis $(\boldsymbol{e}_{r_A}, \boldsymbol{e}_{\varphi_A}, \boldsymbol{e}_{B_A})$, one first determines the intersection M between the helical line passing through M_0 and the plane $\Pi_\perp$, where the velocity is

$$\boldsymbol{u}(\mathrm{M}) = u_\rho(\mathrm{M})\boldsymbol{e}_\rho(\mathrm{M}) + u_\psi(\mathrm{M})\boldsymbol{e}_\psi(\mathrm{M}) + u_b(\mathrm{M})\boldsymbol{e}_b(\mathrm{M}). \tag{C6}$$

The helical symmetry implies that $\boldsymbol{u}(\mathrm{M})$ has the same components as $\boldsymbol{u}(\mathrm{M}_0)$ in the helical basis $(\boldsymbol{e}_r, \boldsymbol{e}_\varphi, \boldsymbol{e}_B)$

$$\boldsymbol{u}(\mathrm{M}) = u_r(\mathrm{M}_0)\boldsymbol{e}_r(\mathrm{M}) + u_\varphi(\mathrm{M}_0)\boldsymbol{e}_\varphi(\mathrm{M}) + u_B(\mathrm{M}_0)\boldsymbol{e}_B(\mathrm{M}). \tag{C7}$$

Projected on the basis $(\boldsymbol{e}_{r_A}, \boldsymbol{e}_{\varphi_A}, \boldsymbol{e}_{B_A})$, this yields

$$\begin{pmatrix} u_{r_A}(\mathrm{M}) \\ u_{\varphi_A}(\mathrm{M}) \\ u_{B_A}(\mathrm{M}) \end{pmatrix} = \left[u_r(\mathrm{M}_0)\boldsymbol{e}_r(\mathrm{M}) + u_\varphi(\mathrm{M}_0)\boldsymbol{e}_\varphi(\mathrm{M}) + u_B(\mathrm{M}_0)\boldsymbol{e}_B(\mathrm{M}) \right] \cdot \begin{pmatrix} \boldsymbol{e}_{r_A} \\ \boldsymbol{e}_{\varphi_A} \\ \boldsymbol{e}_{B_A} \end{pmatrix}. \tag{C8}$$

Using relations

$$\left.\begin{aligned} \boldsymbol{e}_r(\mathrm{M}) \cdot \boldsymbol{e}_{r_A} &= \cos(\theta_M - \theta_A), \\ \boldsymbol{e}_\varphi(\mathrm{M}) \cdot \boldsymbol{e}_{r_A} &= \alpha_M \sin(\theta_A - \theta_M), \\ \boldsymbol{e}_B(\mathrm{M}) \cdot \boldsymbol{e}_{r_A} &= \alpha_M \frac{r_M}{L} \sin(\theta_A - \theta_M), \end{aligned}\right\} \tag{C9}$$

$$\left.\begin{aligned} \boldsymbol{e}_r(\mathrm{M}) \cdot \boldsymbol{e}_{\varphi_A} &= \alpha_A \sin(\theta_M - \theta_A), \\ \boldsymbol{e}_\varphi(\mathrm{M}) \cdot \boldsymbol{e}_{\varphi_A} &= \alpha_M \alpha_A \left[\frac{r_M r_A}{L^2} + \cos(\theta_M - \theta_A) \right], \\ \boldsymbol{e}_B(\mathrm{M}) \cdot \boldsymbol{e}_{\varphi_A} &= \alpha_M \alpha_A \left[-\frac{r_A}{L} + \frac{r_M}{L} \cos(\theta_M - \theta_A) \right], \end{aligned}\right\} \tag{C10}$$

$$\left.\begin{aligned} \boldsymbol{e}_r(\mathrm{M}) \cdot \boldsymbol{e}_{B_A} &= \alpha_A \frac{r_A}{L} \sin(\theta_M - \theta_A), \\ \boldsymbol{e}_\varphi(\mathrm{M}) \cdot \boldsymbol{e}_{B_A} &= \alpha_M \alpha_A \left[-\frac{r_M}{L} + \frac{r_A}{L} \cos(\theta_M - \theta_A) \right] \\ \boldsymbol{e}_B(\mathrm{M}) \cdot \boldsymbol{e}_{B_A} &= \alpha_M \alpha_A \left[1 + \frac{r_M r_A}{L^2} \cos(\theta_M - \theta_A) \right] \end{aligned}\right\} \tag{C11}$$

https://doi.org/10.1017/jfm.2022.500 Published online by Cambridge University Press

as well as, at point M,

$$u_\rho = \cos\psi\ u_{r_A} + \sin\psi\ u_{\varphi_A}, \quad u_\psi = -\sin\psi\ u_{r_A} + \cos\psi\ u_{\varphi_A}, \tag{C12a,b}$$

one obtains (Selçuk 2016)

$$\begin{aligned} u_\rho(\mathrm{M}) = {} & u_r(\mathrm{M}_0)\left[\cos(\theta_M-\theta_A)\cos\psi + \alpha_A\sin(\theta_M-\theta_A)\sin\psi\right] \\ & + u_\varphi(\mathrm{M}_0)\alpha_M\left[\sin(\theta_A-\theta_M)\cos\psi + \alpha_A\left(\frac{r_M r_A}{L^2}+\cos(\theta_M-\theta_A)\right)\sin\psi\right] \\ & + u_B(\mathrm{M}_0)\frac{\alpha_M}{L}\left[r_M\sin(\theta_A-\theta_M)\cos\psi + \alpha_A(-r_A + r_M\cos(\theta_M-\theta_A))\sin\psi\right], \end{aligned} \tag{C13}$$

$$\begin{aligned} u_\psi(\mathrm{M}) = {} & u_r(\mathrm{M}_0)\left[-\cos(\theta_M-\theta_A)\sin\psi + \alpha_A\sin(\theta_M-\theta_A)\cos\psi\right] \\ & + u_\varphi(\mathrm{M}_0)\alpha_M\left[-\sin(\theta_A-\theta_M)\sin\psi + \alpha_A\left(\frac{r_M r_A}{L^2}+\cos(\theta_M-\theta_A)\right)\cos\psi\right] \\ & + u_B(\mathrm{M}_0)\frac{\alpha_M}{L}\left[-r_M\sin(\theta_A-\theta_M)\sin\psi + \alpha_A(-r_A + r_M\cos(\theta_M-\theta_A))\cos\psi\right], \end{aligned} \tag{C14}$$

$$\begin{aligned} u_b(\mathrm{M}) = {} & u_r(\mathrm{M}_0)\alpha_A\frac{r_A}{L}\sin(\theta_M-\theta_A) \\ & + u_\varphi(\mathrm{M}_0)\frac{\alpha_M}{L}\alpha_A[-r_M + r_A\cos(\theta_M-\theta_A)] \\ & + u_B(\mathrm{M}_0)\alpha_M\alpha_A[1+\frac{r_M r_A}{L^2}\cos(\theta_M-\theta_A)]. \end{aligned} \tag{C15}$$

References

Ali, M. & Abid, M. 2014 Self-similar behaviour of a rotor wake vortex core. *J. Fluid Mech.* **740**, R1.

Batchelor, G.K. 1964 Axial flow in trailing line vortices. *J. Fluid Mech.* **20**, 645–658.

Batchelor, G.K. 1967 *An Introduction to Fluid Dynamics*. Cambridge University Press.

Bernoff, A.J. & Lingevitch, J.F. 1994 Rapid relaxation of an axisymmetric vortex. *Phys. Fluids* **6** (11), 3717–3723.

Blanco-Rodríguez, F.J. & Le Dizès, S. 2016 Elliptic instability of a curved batchelor vortex. *J. Fluid Mech.* **804**, 224–247.

Blanco-Rodríguez, F.J. & Le Dizès, S. 2017 Curvature instability of a curved batchelor vortex. *J. Fluid Mech.* **814**, 397–415.

Blanco-Rodríguez, F.J., Le Dizès, S., Selçuk, C., Delbende, I. & Rossi, M. 2015 Internal structure of vortex rings and helical vortices. *J. Fluid Mech.* **785**, 219–247.

Brynjell-Rahkola, M. & Henningson, D.S. 2020 Numerical realization of helical vortices: application to vortex instability. *Theor. Comput. Fluid Dyn.* **34**, 1–20.

Callegari, A.J. & Ting, L. 1978 Motion of a curved vortex filament with decaying vortical core and axial velocity. *SIAM J. Appl. Maths* **35** (1), 148–175.

Cheng, M., Lou, J. & Lim, T.T. 2010 Vortex ring with swirl: a numerical study. *Phys. Fluids* **22** (9), 097101.

Delbende, I., Rossi, M. & Daube, O. 2012 DNS of flows with helical symmetry. *Theor. Comput. Fluid Dyn.* **26** (1), 141–160.

Fukumoto, Y. & Miyazaki, T. 1991 Three-dimensional distortions of a vortex filament with axial velocity. *J. Fluid Mech.* **222**, 369–416.

Fukumoto, Y. & Moffatt, H.K. 2000 Motion and expansion of a viscous vortex ring. Part 1. A higher-order asymptotic formula for the velocity. *J. Fluid Mech.* **417**, 1–45.

Fukumoto, Y. & Okulov, V.L. 2005 The velocity field induced by a helical vortex tube. *Phys. Fluids* **17** (10), 107101.

Hardin, J.C. 1982 The velocity field induced by a helical vortex filament. *Phys. Fluids* **25** (11), 1949–1952.

https://doi.org/10.1017/jfm.2022.500 Published online by Cambridge University Press

HATTORI, Y. & FUKUMOTO, Y. 2014 Modal stability analysis of a helical vortex tube with axial flow. *J. Fluid Mech.* **738**, 222–249.

HICKS, W.M. 1884 VII. On the steady motion and small vibrations a hollow vortex. *Phil. Trans. R. Soc.* **175**, 161–195.

JIMÉNEZ, J., MOFFATT, H.K. & VASCO, C. 1996 The structure of the vortices in freely decaying two-dimensional turbulence. *J. Fluid Mech.* **313**, 209–222.

JOUKOWSKY, N.E. & VETCHINKIN, V.P. 1929 *Théorie tourbillonnaire de l'hélice propulsive*. Gauthier-Villars.

KIDA, S. 1981 Motion of an elliptic vortex in a uniform shear flow. *J. Phys. Soc. Japan* **50** (10), 3517–3520.

KUIBIN, P.A. & OKULOV, V.L. 1998 Self-induced motion and asymptotic expansion of the velocity field in the vicinity of a helical vortex filament. *Phys. Fluids* **10** (3), 607–614.

LE DIZÈS, S. & VERGA, A. 2002 Viscous interactions of two co-rotating vortices before merging. *J. Fluid Mech.* **467**, 389–410.

LESSEN, M., SINGH, P.J. & PAILLET, F. 1974 The stability of a trailing line vortex. Part 1. Inviscid theory. *J. Fluid Mech.* **63**, 753–763.

LEVY, H. & FORSDYKE, A.G. 1928 The steady motion and stability of a helical vortex. *Proc. R. Soc. Lond.* A **120** (786), 670–690.

MAYER, E.W. & POWELL, K.G. 1992 Viscous and inviscid instabilities of a trailing vortex. *J. Fluid Mech.* **245**, 91–114.

MOORE, D.W. & SAFFMAN, P.G. 1972 The motion of a vortex filament with axial flow. *Phil. Trans. R. Soc.* A **272** (1226), 403–429.

OKULOV, V.L. 2004 On the stability of multiple helical vortices. *J. Fluid Mech.* **521**, 319–342.

OKULOV, V.L., KABARDIN, I.K., MIKKELSEN, R.F., NAUMOV, I.V. & SØRENSEN, J.N. 2019 Helical self-similarity of tip vortex cores. *J. Fluid Mech.* **859**, 1084–1097.

OKULOV, V.L. & SØRENSEN, J.N. 2020 The self-induced motion of a helical vortex. *J. Fluid Mech.* **883**, A5.

QUARANTA, H.U., BRYNJELL-RAHKOLA, M., LEWEKE, T. & HENNINGSON, D.S. 2019 Local and global pairing instabilities of two interlaced helical vortices. *J. Fluid Mech.* **863**, 927–955.

RICCA, R.L. 1994 The effect of torsion on the motion of a helical vortex filament. *J. Fluid Mech.* **273**, 241–259.

ROSSI, M. 2000 Of vortices and vortical layers: an overview. In *Vortex Structure and Dynamics* (ed. A. Maurel & P. Petitjeans), Lecture notes in Physics, pp. 40–123. Springer.

SELÇUK, C. 2016 Numerical study of helical vortices and their instabilities. Phd thesis, Université Pierre et Marie Curie, Paris, France.

SELÇUK, C., DELBENDE, I. & ROSSI, M. 2017 Helical vortices: quasi-equilibrium states and their time evolution. *Phys. Rev. Fluids* **2** (8), 084701.

SHTORK, S.I., GESHEVA, E.S., KUIBIN, P.A., OKULOV, V.L. & ALEKSEENKO, S.V. 2020 Parametric description of the stationary helical vortex in a hydrodynamic vortex chamber. *J. Appl. Mech. Tech. Phys.* **61** (3), 359–367.

https://doi.org/10.1017/jfm.2022.500 Published online by Cambridge University Press